1   Word Count: 12,103

2   Revision 1

3   Wenjiite, $Ti_{10}(Si,P,\square)_7$, and kangjinlaite, $Ti_{11}(Si,P)_{10}$, new minerals in the

4   ternary Ti-P-Si system from the Luobusa ophiolite, Tibet, China

5

6   Fahui Xiong[1,2], Xiangzhen Xu[1,2], Enrico Mugnaioli[3], Mauro Gemmi[3], Richard Wirth[4], Jingsui

7   Yang[1,5] and Edward S. Grew[6*]

8

9   [1]Center for Advanced Research on the Mantle (CARMA), *Key Laboratory of Deep-Earth*

10   Dynamics of Ministry of Land and Resources, Institute of Geology, Chinese Academy of

11   Geological Sciences, Beijing 100037, China

12   [2]Southern Marine Science and Engineering Guangdong Laboratory (Guangzhou)，511458,

13   China

14   [3]Center for Nanotechnology Innovation@NEST, Istituto Italiano di Tecnologia (IIT), Piazza San

15   Silvestro 12, 56127 Pisa, Italy

16   [4]Helmholtz Centre Potsdam, GFZ (German Research Centre for Geosciences), 3.5 Surface

17   Geochemistry, Telegrafenberg, C 120, D-14473 Potsdam, Germany

18   [5]School of Earth Sciences and Engineering, Nanjing University, Nanjing, 210023, China.

19   [6]School of Earth and Climate Sciences, University of Maine, Orono, Maine 04469 USA

20   E-mail: esgrew@maine.edu

21

22   ABSTRACT

23 The new minerals wenjiite, $Ti_{10}(Si,P,\square)_7$ (IMA2019-107c) and kangjinlaite, $Ti_{11}(Si,P)_{10}$

24 (IMA2019-112b) occur with badengzhuite, zhiqinite and a K-bearing dmisteinbergite-like

25 mineral in a spheroid 20 μm across enclosed in corundum from the Cr-11 podiform chromitite

26 orebody near Kangjinla, Luobusa ophiolite, Tibet, China. In addition, wenjiite occurs with

27 deltalumite, jingsuiite, osbornite-khambaraevite and the K-bearing dmisteinbergite-like mineral

28 in a lamellar intergrowth 100 μm long, also enclosed in corundum from the same locality. The

29 new minerals were characterized by energy-dispersive spectroscopy and three-dimensional

30 electron diffraction, which enabled us to obtain an ab-initio structure solution and dynamical

31 refinement from grains a few μm across hosted in a FIB lamella. Four analyses of wenjiite from

32 the spheroid gave in wt% Si 21.67, P 6.24, Ti 66.39, V 1.37, Cr 2.20, Mn 0.97, Fe 1.17, total 100

33 (normalized), which corresponds to $(Ti_{0.93}Cr_{0.03}Mn_{0.01}Fe_{0.01}V_{0.02})_{10}(Si_{0.79}P_{0.21})_{6.51}$ on the basis of

34 10 cations excluding Si and P. The simplified formula is $Ti_{10}(Si,P)_{6.5}$, or more generally $Ti_{10}Si_xP_y$,

35 where x > y and $6 \leq (x + y) \leq 7$, i.e., $Ti_{10}(Si,P,\square)_7$. Wenjiite has hexagonal symmetry, space

36 group: $P6_3/mcm$ (#193), with $a = 7.30(10)$ Å, $c = 5.09(10)$ Å, $V = 235(6)$ Å^3, $Z = 1$, and is

37 isostructural with xifengite, mavlyanovite, synthetic Ti_5Si_3 and synthetic $Ti_5P_{3.15}$. Four analyses

38 of kangjinlaite gave in wt% Si 25.56, P 9.68, Ti 62.35, V 0.21, Cr 0.83, Mn 0.42, Fe 0.95, total

39 100 (normalized), which corresponds to $(Ti_{10.65}V_{0.03}Cr_{0.13}Mn_{0.06}Fe_{0.14})_{\Sigma11.01}(Si_{7.43}P_{2.55})_{\Sigma9.99}$. The

40 simplified formula is $Ti_{11}(Si,P)_{10}$. Kangjinlaite is tetragonal, with space group: $I4/mmm$ (#139), a

41 $= 9.4(2)$ Å, $c = 13.5(3)$ Å, $V = 1210(50)$ Å^3, $Z = 4$, and is isostructural with synthetic compounds

42 of the $Ho_{11}Ge_{10}$ type, being the most compact of these phases. Despite there now being over 70

43 compounds containing 38 elements isostructural with $Ho_{11}Ge_{10}$, synthesis of an analogue of

44 kangjinlaite has not been previously reported in either the Ti-P or Ti-Si binary systems or in a

45 multicomponent system. The previously deduced crystallization sequence with decreasing

46 temperature of the 4 minerals in the spheroid wenjiite → kangjinlaite → zhiqinite +

47 badengzhuite is consistent with relationships reported in 9 binary systems containing

48 intermetallic compounds of Ge and Sn isostructural with Mn_5Si_3 and $Ho_{11}Ge_{10}$, in 8 of which the

49 Mn_5Si_3 analogue melts congruently, whereas the $Ho_{11}Ge_{10}$ analogue never does. Instead the

50 $Ho_{11}Ge_{10}$ analogue melts peritectically, generally to an Mn_5Si_3 analogue and less commonly to

51 compounds with 5:4 stoichiometry. Final crystallization of the spheroid to zhiqinite +

52 badengzhuite is expected to be well below the temperature of 1500 °C for the congruent melting

53 of zhiqinite in the Ti-Si system, i.e. in the range of ~1100 – 1300 °C.

54

55 **Keywords:** Luobusa chromitite, wenjiite, kangjinlaite, intermetallic melts, crystal structure,

56 transmitting electron microscopy, 3-dimensional electron diffraction

57   *E-mail: esgrew@maine.edu

58   **Introduction**

59 Intermetallic phases are relatively rare in natural systems, being largely restricted to extra-

60 terrestrial environments. Most of these occurrences are dominated by iron, e.g., meteorites,

61 whereas occurrences with minerals dominated by Ti are rare. Notable examples include a

62 fulgurite containing TiP (Essene and Fisher 1986), the type locality for native titanium (Fang et

63 al. 2013; Dobrzhinetskaya et al. 2014) and inclusions in corundum from Mount Carmel, Israel

64 (e.g., Griffin et al. 2020, 2021), and the Luobusa ophiolite, Tibet, China (e.g., Xiong et al. 2020,

65 2021a, 2021b, 2022, this study). Although Ti-bearing intermetallic phases have wide applications

66 and are thus extensively studied, naturally occurring compounds are being reported that have yet

67 to be synthesized.

68

69   Wenjiite and kangjinlaite are two such examples as they are the first ternary solid solutions to be

70   reported in the Ti-Si-P system, either natural or synthetic. End member Ti_5Si_3 was first

71   synthesized by Pietrokowsky and Duwez (1951) and has been widely studied due to its industrial

72   importance as a refractory silicide (e.g. Frommeyer and Rosenkranz, 2004). This end member is

73   isostructural with the minerals xifengite, Fe_5Si_3 (Yu et al. 1984) and mavlyanovite (Yusupov et

74   al. 2009), Mn_5Si_3, as well as with synthetic Ti_5P_{3+x} (Bärnighausen et al. 1965; Lundström and

75   Snell 1967). In contrast, no compound isostructural with kangjinlaite has been reported in either

76   the Ti-P or the Ti-Si system. Instead, kangjinlaite is isostructural with synthetics of the $Ho_{11}Ge_{10}$

77   type, the structure of which was first determined by Smith et al. (1967). At present, the structures

78   of over 70 phases composed of 38 elements have been shown to be isostructural with $Ho_{11}Ge_{10}$.

79   Research on phases of the $Ho_{11}Ge_{10}$ type has been motivated by their potential energy-converting

80   or saving capabilities as magnetocaloric or thermoelectric materials because global demands for

81   alternative energy resources has stimulated a renewed interest in thermoelectric materials for use

82   in power generation (Rauscher et al. 2007; Jeon et al. 2016).

83

84   The present paper describes wenjiite and kangjinlaite, which were reported preliminarily in

85   Xiong et al. (2021a,b). Their characterization as new minerals is largely based on the spheroid in

86   foil #5358, also the holotype specimen for badengzhuite and zhiqinite (Xiong et al. 2020). We

87   consider the implications of wenjiite and kangjinlaite for understanding intermetallic phases for

88   natural parageneses and synthetic assemblages. The structures of both minerals were determined

89   ab-initio and dynamically refined by 3-dimensional electron diffraction (Kolb et al. 2007;

90   Mugnaioli and Gemmi 2018; Gemmi et al. 2019; Steciuk et al. 2019a,b; Mugnaioli et al.

91   2020a,b).

4

92   **Methods**

93   **Preparation of corundum separates from the Cr-11 chromitite body and evidence for a**

94   **natural origin of the corundum**

95   Corundum and the unusual minerals included therein were extracted by processing ~1100 kg of

96   chromitite at the Institute of Multipurpose Utilization of Mineral Resources, Chinese Academy

97   of Geological Sciences, Zhengzhou, including massive, disseminated, and nodular ores from the

98   Cr-11 orebody near Kangjinla, a process carried out with great care as described in detail by Xu

99   et al. (2009, 2015). In brief, the samples were first passed through a jaw crusher and then ground

100   in stages to three sizes, and the minerals were separated from each size fraction by a combination

101   of gravity, magnetic and electrostatic techniques. The mineral concentrates were handpicked

102   under a binocular microscope, and the selected minerals mounted in epoxy and then ground to

103   about half their thickness. The grains were polished using man-made diamond grinding grease

104   and cleaned in an ultrasonic bath. As far as we are aware, no industrial alumina was used at any

105   stage of the extraction process.

106   Despite the assertions that contamination of the separates was unlikely, the occurrence of highly

107   reduced phases in the Luobusa ophiolite remains controversial. Litasov et al. (2019a,b)

108   contended that the separates were contaminated by brown fused alumina used in abrasives,

109   whereas Ballhaus et al. (2017, 2018, 2021) argued formation of the highly reduced phases at

110   mantle depths was unlikely. After reviewing the arguments for and against a natural origin,

111   Xiong et al. (2020, 2022) concluded the preponderance of evidence favored a natural origin of

112   the corundum grains and the highly reduced phases enclosed in these grains from the Cr-11

113   chromitite deposit.

114

Transmission electron microscopy and the focused ion beam technique

115

116   At the GFZ Potsdam, transmission electron microscopy (TEM) and the focused ion beam (FIB)

117   technique (for details of method in general, see Wirth 2004, 2009) were used to prepare foils

118   #5357, #5358 and #6034 for subsequent EDX and 3-dimensional electron diffraction analysis at

119   the Istituto Italiano di Tecnologia. TEM requires that samples be prepared as foils sufficiently

120   thin to be transparent to electrons (generally, the foil thickness is less than 200 nm). Electron

121   transparent foils were prepared with a FIB. Typical TEM foils have the dimensions 15×10×0.20

122   μm. A FIB single beam device (FEI FIB 200 TEM) was used for sample preparation. For this, a

123   Ga-ion beam (30 keV acceleration voltage) is focused onto a selected location of the sample

124   surface to sputter material from the sample. We exclude the possibility that FIB preparation can

125   induce a phase transition in an intermetallic phase such as wenjiite or kangjinlaite. In addition,

126   amorphisation was never detected in our samples.

127

Energy dispersive X-ray analyses

128

129   Chemical analyses of minerals in foils #5358 and #6034 were carried out at the Istituto Italiano

130   di Tecnologia (IIT), Center for Nanotechnology Innovation@NEST, Pisa, using energy

131   dispersive X-ray spectroscopy (EDX) with a Bruker EDX XFlash6T-60 detector mounted on a

132   Zeiss Libra TEM operating at 120 kV.

133

134   EDX quantifications used the thin-specimen approximation by Cliff and Lorimer (1975). We did

135   not use standards, consequently the reported weight percent derive from the initial calibration of

136   the instrument. The absence of any significant drift is evident in the precision of the analyses at 4

137   closely spaced analyses of wenjiite (Fig. 1), that is, the 1-sigma errors range mostly 4-10 % for

138   the three major constituents, Si, P and Ti at each of the 4 spots analysed over a 6-month period

139   from June to December, 2019 (columns 1-4 in Table 1) and mostly from 3 to 10 wt % for an

140   average of all 4 spots analysed (column 5, Table 1). Similarly, the absence of significant drift

141   over the 6-month period that kangjinlaite was analysed is evident in the precision of the analyses

142   at 4 closely spaced analytical spots (Fig. 1). That is, the 1-sigma errors range from 4 to 8 wt% for

143   the three major constituents, Si, P and Ti at each of the 4 spots analysed (columns 1-4 in Table 2)

144   and from 3 to 7 wt % for an average of all 4 spots analysed (column 5, Table 2). Since the

145   precision for the average analysis is the same as for the individual analyses of both minerals, we

146   conclude that there was negligible drift over this 6-month period.

147

148   Although the EDX analyses of wenjiite and kangjinlaite were standardless, badengzhuite and

149   zhiqinite analysed concurrently with kangjinlaite on June 27, 2019 could be used as internal

150   standards because of their simple stoichiometry, TiP and $TiSi_2$, respectively. The results on these

151   internal standards give their stoichiometry as close to ideal, $Ti_{1:020}P_{0:980}$ and $Ti_{0:905}Si_{2:095}$,

152   respectively (Xiong et al. 2020). Since there is no evidence for significant drift, data on the

153   internal standards at one session can be applied to other sessions.

154

155   **Three-dimensional electron diffraction and structure analysis**

156   3-dimensional electron diffraction (3D ED) data (Gemmi et al. 2019) were acquired on foils

157   #5357, #5358, and #6034 with a Zeiss Libra TEM operating at 120 kV and equipped with a LaB_6

158   source at the Istituto Italiano di Tecnologia (IIT), Center for Nanotechnology Innovation@NEST,

159   Pisa, whereas structure analysis was carried out only on foil #5358 (Fig. 1). 3D ED was

160   performed in STEM mode after defocusing the beam in order to have a parallel Köhler

161   illumination on the spot being analyzed. A beam size of about 150 nm in diameter was obtained

162 by inserting a 5 μm C2 condenser aperture. An extremely low dose illumination was used in

163 order to avoid any possible amorphization of the sample. A 150 nm diameter beam results in a

164 considerable reduction of resolution. Nonetheless, we can generally see features of few hundreds of

165 nanometers across, because the STEM step is still very small. For foil #5358, difficulties for crystal

166 tracking were not connected with the defocusing of the beam, but with the different phases having a

167 similar density, which mostly determines contrast in STEM. Fortunately, dimensions of the areas for

168 wenjiite and kangjinlaite are large compared to our 150 nm beam, and no reduction of data quality is to be

169 expected. In contrast, analyzing badengzhuite (TiP) and zhiqinite ($TiSi_2$) in the same FIB lamella was a

170 challenge (Xiong et al. 2020). For both wenjiite and kangjinlaite data were collected in a relatively thin

171 area close to the FIB lamella edge, still a greater thickness than conventional powdered samples has to be

172 expected. This increases the relative amount of dynamical scattering.

173

174

175 The best data for use in structure solution and refinements were collected from foil #5358 using

176 an angular step of 1° and in total tilt range of 110° (from -50° to +60°), using an omega energy-

177 filter for cutting-out the inelastic scattering. After each tilt, a diffraction pattern was acquired and

178 crystal position tracked by defocused STEM imaging. During the experiment, the beam was

179 precessed around the optical axis by an angle of 1° (Vincent and Midgley 1994), as first

180 described by Mugnaioli et al. (2009). Precession was obtained using a Nanomegas Digistar

181 P1000 device. Diffraction patterns were recorded by an ASI Timepix single-electron camera

182 (Nederlof et al. 2013).

183 3D ED data were analyzed using the software PETS (Palatinus *et al.* 2019). Ab-initio structure

184 determination was obtained by standard direct methods (SDM) as implemented in the software

185 SIR2014 (Burla et al. 2015). Data were treated with a fully kinematical approximation, i.e.

8

186 neglecting dynamical scattering and assuming that I_{hkl} was proportional to $|F_{hkl}|^2$. Least-squares

187 structure refinement was performed with the software JANA2006 (Petříček et al. 2014) using the

188 dynamical refinement procedure described by Palatinus *et al.* (2015a,b). For kangjinlaite all

189 available 111 diffraction patterns were used for the refinement, whereas for wenjiite 18 patterns

190 were discarded due to bad quality. Some thermal parameters, especially for Ti, tend to turn

191 negative during dynamical refinement. Therefore, all thermal parameters were constrained to the

192 value 0.005 $Å^2$

193 More details about structure determination and refinement are reported in the supplements

194 (Tables S1 and S2).

195 The visualization of the 3D ED data was obtained by the software ADT3D (Kolb et al. 2011) and

196 structure sketches were drawn by the software VESTA (Momma and Izumi 2011).

197

Powder pattern

199 X-ray powder diffraction data for wenjiite (Appendix Table S3 and Figure S1) and kangjinlaite

200 (Table S4 and Figure S2) were obtained by simulation in Debye-Scherrer geometry with a

201 monochromatic Cu $K\alpha_1$ radiation (λ=1.540598) using the software PowderCell 2.4.

202

Electron Backscattered Diffraction (EBSD)

204 EBSD was used for the identification of wenjiite and associated minerals in sample G7708 only.

205 Sample surface preparation included stepwise diamond polishing followed by a 30–45 minute

206 chemo-mechanical polishing step in a suspension of sequential 25 nm, 10 nm and 5nm colloidal

207 silica (pH 9.8) to eliminate any mechanical damage. No carbon coating was applied in order to

208 guarantee optimum Kikuchi diffraction pattern quality. Data were acquired using a field

209   emission scanning electron microscope (FEI-SEM Quanta450) equipped with the Nordlys Max2

210   EBSD camera commercialized by Oxford Instruments, housed in Institute of Geology, Chinese

211   Academy of Geological Sciences. The microscope working conditions were the same for all

212   analyses, with an acceleration voltage of 20 kV, a probe current of ~1.1 nA, a stage tilt of 70°,

213   and a working distance of 23 mm.

214

215   **Mineral names and deposition of holotype material**

216   The first new mineral and its name, wenjiite, was approved by the IMA CNMNC (IMA2019-

217   107c) (Xiong et al. 2021a). The mineral is named for Bai Wenji, born in China, Jilin Province,

218   October 15, 1935, and died January 11, 2019. In the literature, his name is written with "Bai" as

219   his surname and "Wenji" as his given name. His professional career began in 1958. He was

220   Research Professor of Institute of Geology, Chinese Academy of Geological Sciences. He was

221   the first person to find diamonds, native Fe and other special minerals in chromitite in the

222   Luobusa ophiolite in 1981. He carried out detailed research on many suture zone ophiolite

223   chromitites in China, including Dongqiao, Hegenshan and Sartuohai. He discovered and named 7

224   new mineral species and was first or second author on the articles reporting them, including

225   luobusaite, linzhiite, naquite, zangboite, yarlongite, qusongite, native titanium. He was also the

226   first or co-author of about 50 papers and two Chinese Geologic Books.

227   The second new mineral and its name, kangjinlaite, was approved by the IMA CNMNC

228   (IMA2019-112b) (Xiong et al. 2021b). The mineral is named for Kangjinla, the district in which

229   the chromitite orebody Cr-11 is located.

230   The holotype specimen of both wenjiite and kangjinlaite has been submitted to the Chinese

231   Geological Museum, Xisiyangrouhutong 15th, Xicheng District, Beijing, China. The number

232 assigned to this specimen is M16104 (source of foil no. 5358). Foil no. 5358, designated as the

233 holotype sample of both minerals, is to be kept with the specimens in the Chinese Geological

234 Museum.

235

236 **Results**

237 **Occurrence and morphology**

238 Wenjiite and kangjinlaite occur in the Cr-11 orebody, one of several significant chromitite

239 deposits in the Luobusa ophiolite, which is located about 200 km east-southeast of Lhasa. The

240 Cr-11 orebody, elevation of 5 300 m, is located at 29°11′ N, 92°18′ E, is the largest ore body of

241 the Kangjinla mining area, and now has an increase of 300,000 tons of reserves. The orebody Cr-

242 11 is a podiform body, 0.3–10.5 m thick, at least a length of 330m now, which strikes 105° and

243 dips 50°–72° SW. Rutile and REE minerals were found as inclusions in corundum from Cr-11.

244

245 Wenjiite is found in several inclusions, together with kangjinlaite in one, of highly reduced

246 compounds enclosed in corundum. Identification was confirmed by 3-dimensional electron

247 diffraction data obtained at one point each in foils #5358 (holotype, Fig. 1), #5357 (Xiong et al.

248 2022, Fig. 4) and #6034 (Fig. 2), and by electron backscattered diffraction in G7708 (Fig. 3).

249 There are four modes of occurrence for wenjiite and one of kangjinlaite:

250 ---(1) Wenjiite and kangjinlaite together constitute about 50% of a spheroid 20 μm across

251 enclosed in corundum (brighter patches in BSE image in the inset, Fig. 1). Zhiqinite, $TiSi_2$,

252 constitutes much of the remainder of the spheroid (less bright phase in BSE image). Wenjiite and

253 kangjinlaite cannot be distinguished visually in the high-angle annular dark-field scanning-

254 transmission electron microscope (HAADF-STEM) image; chemical analyses and electron

255 diffraction were required to distinguish them. The two minerals are readily distinguished from

256 zhiqinite, which forms an aggregate composed of individual grains mostly 1 to 2 μm long,

257 several of which have a tabular habit. The zhiqinite aggregate encloses globules ≤1 μm across of

258 badengzhuite, TiP. A K-bearing dmisteinbergite-like mineral has a direct contact with wenjiite.

259 Xu et al. (2018) illustrated a similar spheroid ~15 μm in diameter from the same locality. It is

260 composed of two grains ~5 μm across of Ti-Si-P that could be wenjiite and kangjinlaite

261 surrounded by a matrix rich in Si, most likely zhiqinite, studded with grains < 1 μm across rich

262 in P, presumably badengzhuite. Electron microprobe analyses reported by Xu et al. (2018) are

263 consistent with these provisional identifications.

264 ---(2) An incomplete overgrowth of wenjiite up to 20 μm thick around a jingsuiite grain about 40

265 μm across in association with osbornite-khamrabaevite (Xiong et al. 2022, Fig. 4).

266 ---(3) A platelet of wenjiite flattened // (100) occurs in a lamellar intergrowth with jingsuiite,

267 khamrabaevite-osbornite and deltalumite, $(Al, Mg, \square)Al_2O_4$, in foil #6034 (Fig. 2). The relative

268 orientation of the phases was determined by 3-dimensional electron diffraction to be jingsuiite

269 (001) // khamrabaevite-osbornite (111) // deltaluminite (111) // interstitial K-bearing

270 dmisteinbergite-like mineral (001) //wenjiite (100). The surrounding corundum areas all have the

271 same orientation, which implies that these areas belong to a single crystal. However, the

272 crystallographic orientation of corundum does not appear to be related to the crystallographic

273 orientations of the inclusions.

274 ---(4) Wenjiite forms two grains up to 20 μm in the longest dimension (Fig. 3) with osbornite and

275 a Ti-Zr-Al-Si oxide close to carmeltazite in stoichiometry. However, attempts to confirm

276 identification as carmeltazite using EBSD were not successful as matches for kangjinlaite and

277 Ti_5Si_4 as well as for carmeltazite were obtained. Jingsuiite is also present, but not in contact with

278   wenjiite.

279

280   Nowotny et al. (1959, Fig. 1) synthesized 6-sided prismatic crystals of the end member

281   composition Ti_5Si_3 by sublimation from a gas phase. The crystals are 0.5 mm across and 5 mm

282   long (elongation // [001]) and are terminated by pyramidal faces. Frommeyer and Rosenkranz

283   (2004) reported twinning in the synthetic Ti_5Si_3 end member, but none has been found in natural

284   wenjiite.

285

286   **Physical and optical properties**

287   The natural material is too fine-grained for physical properties to be observable, but properties

288   have been reported from synthetic wenjiite. No synthetic analogue is available for kangjinlaite as

289   this compound has never been synthesized. Synthetic end member wenjiite (Ti_5Si_3) is silvery

290   gray (Krikorian, 1955), whereas Hahn and Ness (1957) reported sublimation of synthetic

291   wenjiite to a thin violet film or to a silvery gray coating of crystals. The lustre is metallic

292   (Krikorian, 1955). The hardness (Mohs) is 6½ as estimated from the Vickers hardness (Micro-

293   indentation) of 970 ± 20 in Vickers scale (load 1 kp Frommeyer and Rosenkranz, 2004). The

294   densities calculated from cell parameters, structural model and EDX data are 4.762 g·cm^{-3} for

295   wenjiite and 4.538 g·cm^{-3} for kangjinlaite. The measured density is reported to be 4.32 g·cm^{-3} for

296   end member Ti_5Si_3 (Frommeyer and Rosenkranz, 2004).

297

298

299   **Chemical composition**

300   Wenjiite was analysed at 4 spots in foil #5358 (Fig.1, Table 1), the holotype sample, and at 4

13

301   spots on foil #6034 (Fig. 2, Table 3). EDX spectra revealed the presence of Si, P, Ti, V, Cr, Mn

302   and Fe in both minerals. Relatively few net counts of O were detected during EDX analyses

303   (Tables 1, 3), and we conclude that O is not present, and by extension, neither H_2O nor CO_2 is

304   present.

305

306   The two EDX chemical analyses numbered 413 and 466 and the 3-dimensional diffraction data

307   of wenjiite were collected within the area marked by the large white square in Figure 1 or very

308   close, whereas the two analyses numbered C31 and C32 were collected within 1 μm. The two

309   sets of EDX analyses are nearly identical. We believe that we are justified in concluding there is

310   complete crystallographic continuity in the immediate vicinity of the square, and thus all four

311   EDX analyses were obtained on the same crystal and could be averaged (Fig. 1).

312

313   The empirical formulae for the averages calculated on the basis of 10 cations excluding Si and P,

314   a normalization consistent with the crystallographic data, yielded

315    $(Ti_{0.93}Cr_{0.03}Mn_{0.01}Fe_{0.01}V_{0.02})_{10}(Si_{0.79}P_{0.21})_{6.51}$ for wenjiite in foil #5358. The ideal formula based

316   on this average is $Ti_{10}Si_xP_y$, where $x > y$ and $6 \leq (x + y) \leq 7)$. The end member $Ti_{10}Si_6$ requires Ti

317   73.96, Si 26.04, Total 100 wt%. The ideal formula can also be written $Ti_{10}(Si,P,\square)_7$ where $0 \leq \square$

318   ≤ 1 on the basis of the crystal structure, that is, $\square \approx 0.5$ for wenjiite in foil #5358. In contrast the

319   4 analyses of wenjiite in foil #6034 give an average of $Ti_{0.90}Cr_{0.03}Fe_{0.06}Mn_{0.01})_{10}(Si_{0.65}P_{0.35})_{5.72}$,

320   that is, Si + P < 6 per formula unit (Fig. 4). However, EDX analyses on foil #6034 were done

321   with a non-analytical TEM holder, and therefore a small increase of Ti signal had to be expected.

322   As a result, we will consider only the analyses from foil #5358 in deducing the compositional

323   range of wenjiite.

324

325   Kangjinlaite was analysed at 4 spots in two areas in foil #5358 (Fig. 1, Table 2). The empirical

326   formula calculated on the basis of 21 cations from the average (Fig. 4), a normalization

327   consistent with the crystallographic data indicating that all the Ti and (Si, P) sites are fully

328   occupied, gave $(Ti_{10.65}V_{0.03}Cr_{0.13}Mn_{0.06}Fe_{0.14})_{\Sigma 11.01}(Si_{7.43}P_{2.55})_{\Sigma 9.99}$. The simplified formula is

329    $Ti_{11}(Si,P)_{10}$, and the ideal end member formula is $Ti_{11}Si_{10}$, which requires Ti 65.21, Si 34.79,

330   Total 100 wt%. Kangjinlaite has a higher $X_P = P/(P + Si)$ [atomic] than associated wenjiite (Fig.

331   4).

332

Powder X-ray diffraction patterns

334   The simulated powder X-ray powder patterns are included in the supplements (Tables S1 and S2;

335   Fig. S1 and S2) to aid investigators identify Ti-Si-P phases in the absence of single-crystal X-ray

336   or electron diffraction data.

337

Wenjiite crystal structure

339   Projections of the 3-dimensional reconstructed diffraction volume for wenjiite in foil #5358 are

340   shown in Figure 5. The input composition was $Ti_{10}Si_{5.4}P_{1.6}$. The 3-dimensional electron

341   diffraction data set collected after energy-filtering the inelastic scattering gave a nice ab-initio

342   structure solution in space group $P6_3/mcm$. This solution showed two sites for Ti and one site for

343   (Si,P); the difference Fourier map shows two significant potentials: one positive close to (0,0,0)

344   and one negative along (⅔,⅓,z).

345   The next step was a dynamical refinement. The negative potential almost disappeared, whereas

346   the positive one got stronger. This is a clear hint of an 'interstitial' atom at (0,0,0). The average

15

347   of 4 EDX analyses suggest for this site an occupancy of 0.51.

348

349   Subsequently an (Si,P) atom was placed at (0,0,0) and refined again. In the first attempt we

350   constrained only the overall Si:P ratio as determined by EDX and the total occupancy of 0.5 for

351   the "interstitial" Si/P site at (0,0,0), while the Si:P ratio was freely refined for both Si/P sites. In

352   this case the interstitial site is fully occupied by Si. On the other hand, P may be more consistent

353   with the smaller space of the interstitial position, so the structure was refined a second time,

354   keeping the interstitial position fully occupied by P. For a third attempt, the structure was refined

355   so that Si:P ratio was fixed to be the same value for both (Si,P) positions. The output of these

356   three refinements is very close in terms of residual. Therefore we decided to accept the third one

357   (Tables 4, S3) out of caution, that is, in order to avoid extracting from our data more information

358   than we can be confident of extracting. The final agreement factors are: R(3sigma)=0.1258,

359   wR(3sigma)=0.1604; R(all)=0.1970 and wR(all)=0.1707 (see attached CIF). We finally note that

360   the Si2/P2 site is less strictly coordinated than the Si1/P1 and is at least 50% vacant. Considering

361   this situation, we are not surprised to have ended up with an anomalously high thermal parameter

362   for this site.

363

364   An additional refinement was attempted after reducing the symmetry to P-3$_1m$, thereby giving

365   only one interstitial atom per cell, but with full occupancy. This refinement yielded a strong

366   positive potential in the Fourier map exactly where the second interstitial atom is supposed to be.

367   This means that disorder is present at the scale of few tens of nanometers, and therefore $P6_3/mcm$

368   is the correct choice for the space group.

369

370   Further confirmation that the refinement is reasonable is provided by the relative lengths of

371   cation-cation bonds, which are very consistent with bond lengths reported for Ti_5Si_3 and Ti_5P_{3+x}

372   (Table 5). Bonds that are relatively short in the binary compounds are relatively short in wenjiite

373   and conversely, bonds that are relatively long in the binary compounds are relatively long in

374   wenjiite.

375

376   The structure of wenjiite (Fig. 6) hosts two crystallographically independent Ti atoms. Ti1 is

377   coordinated with six (Si,P) atoms inside a rather distorted octahedron. Ti2 is instead coordinated

378   with five fully occupied (Si,P) atoms and two half-occupied interstitial (Si,P) atoms. Both

379   coordination polyhedra are closely packed in a face-sharing configuration. When the interstitial

380   (Si,P) atoms are removed from the structure, we observe a channel at $(0,0,l)$, with a relatively

381   large diameter of about 5.2 Å.

382

383   **Kangjinlaite crystal structure**

384   The three-dimensional electron diffraction data of kangjinlaite were collected from foil #5358

385   (Fig. 1). The input composition was $Ti_{11}(Si_{7.4}P_{2.6})_{\Sigma 10}$.

386

387   The reconstructed 3-dimensional diffraction volume is consistent within experimental error with

388   a F-centered cubic cell having $a = 13.4(3)$ Å (Fig. 7). No further extinction was detected,

389   suggesting the extinction symbol '$F---$'. Structure solutions were attempted in all related

390   space groups ($F23$, Fm-3, $F432$, F-43m and Fm-3m), but no stable and crystal-chemical sensible

391   model could be obtained.

392   Symmetry was then reduced to tetragonal $I4/mmm$, taking into account all the three

17

393   possible axis choices. Only one of these settings, the one with the longest parameter associated

394   with the unique c axis, allowed a consistent structure determination. The resulting cell

395   parameters are $a = 9.4(2)$ Å, $c = 13.5(3)$ Å (Fig. 7).

396   Structure solution was obtained by SIR2014 (Burla et al., 2015) using scattering factors

397   for electrons and kinematical approximation. The potential map showed nine well-resolved

398   peaks. The strongest four peaks were interpreted as Ti positions, while the other five peaks were

399   interpreted as mixed (Si,P) positions. The resulting stoichiometry is $Ti_{11}(Si,P)_{10}$.

400   The structure (Tables 6, 7, S4; Fig. 8) was subsequently refined by both kinematical and

401   dynamical methods, using the software JANA2006 (Petříček et al., 2014; Palatinus et al.,

402   2015a,b). No geometrical restraint or constraint was imposed. In both refinements most of

403   thermal parameters turn negative, arguably as a consequence of the thickness of the FIB lamella

404   from which data were recorded. Dynamical refinement converged with wR(all) = 17.08%. We

405   did not attempt to refine the Si-P distribution due to the close scattering values of these two

406   atomic species.

407

408   The structure of kangjinlaite belongs to the $Ho_{11}Ge_{10}$ type (Smith et al., 1967) and can be

409   described by an assembly of face-sharing coordination polyhedra centered on four

410   crystallographically independent Ti atoms. Ti atoms are coordinated with 7 to 8 (Si,P) atoms,

411   with interatomic Ti-(Si,P) distances ranging between 2.39 and 2.81 Å. Like for all $Ho_{11}Ge_{10}$-type

412   structures, some Ti-Ti and Si-Si interatomic distances are unusually short. In particular, Si1

413   atoms form a squared cluster with side of 2.41 Å, an unusual feature already spotted by Smith et

414   al. (1967) and resembling the aromatic Si4 rings described by Liu & Wang (2018) and the

415   germanium-iron cluster described by Wolf et al. (2013).

416

Discussion

417

Compositional range covered by the mineral wenjiite

418

In defining a compositional range for wenjiite and its P analogue we have taken into

419

consideration the following: (1) crystallographic studies of synthetic P and Si analogues (e.g.,

420

Bärnighausen et al. 1965; Lundström and Snell 1967; Thom et al. 2000; Williams et al. 2000a,b;

421

Bilibrov et al. 2014), (2) compositional data on the synthetic Ti-Si and Ti-P binary analogues of

422

wenjiite (Fiore et al., 2016; Okamoto, 2007) and (3) compositional and crystallographic data

423

obtained on naturally occurring ternary wenjiite (this study). After consideration of these studies,

424

we propose the formula $Ti_{10}Si_xP_y$, where $6 \leq (x + y) \leq 7$, i.e., $Ti_{10}(Si,P,\square)_7$ with $0 \leq \square \leq 1$, for

425

wenjiite. This formula expresses the potential compositional range for wenjiite and its P-

426

dominant analogue (Fig. 4).

427

428

The upper limit of Si + P = 7 ($\square$ = 0) per formula unit proposed for wenjiite and its P analogue is

429

dictated by occupancy of the interstitial (0, 0, 0) site (Si2/P2 in Table 5). There is no

430

crystallographic evidence for $\square$ > 1, i.e., for vacancies at the Si1/P1 site either in published

431

refinements or in our own structure refinement. Synthetic compounds incorporating elements at

432

the interstitial site have been extensively studied and have been given the formula $Ti_{10}Si_6X_2$,

433

where X denotes the occupant of the interstitial site and includes B, C, N or O (e.g., Thom et al.

434

2000; Williams et al. 2000a; Bilibrov et al. 2014, Corbett 2000; Corbett et al. 1998). In most

435

cases, the interstitial site in these compounds is not more than 50% occupied, that is one atom of

436

B, C, N or O per formula unit or $Ti_{10}Si_6X_1$ (e.g., Thom et al. 2000; Williams et al. 2000a).

437

438

439   J.D. Corbett and E.A. León-Escamilla have also discussed occupancy of the interstitial site by H

440   (Corbett and León-Escamilla 2003; León-Escamilla and Corbett 2006). However, it does not

441   appear that the presence of H was determined crystallographically; X-ray diffraction was used

442   only for measuring accurate cell parameters, and the synthesized products were not chemically

443   analyzed. In our case we have no evidence of H in any of the surrounding phases, that is,

444   kangjinlaite, zhiqinite or badengzhuite, do not contain H. Thus, we conclude H plays a

445   subordinate, if any, role in wenjiite. Instead, X = Si and/or P, in which case the interstitial site is

446   expected not to be more than 50% occupied because of the very short (Si,P)2-Ti distance of 2.16

447   Å (Table 5). This constraint is consistent with the 15-31% P occupancy reported by

448   Bärnighausen et al. (1965) and Lundström and Snell (1967) and by the maximum Si content not

449   exceeding 7 (Si, P) per formula unit in wenjiite from foil #5358 (Fig. 4).

450

451   Determining the lower limit of (Si + P) in wenjiite is more problematic. As noted above, there

452   are no reports of vacancies at Si1/P1 sites, and thus setting Si + P = 6 ($\square$ = 1) as the lower limit

453   for Si + P is our choice for wenjiite and its P analogue despite this limit not being consistent with

454   available compositional data on the binary Ti-Si and Ti-P analogues of wenjiite. These data

455   reveal deviations from the ideal stoichiometry of $Ti_{10}Si_6$ and $Ti_{10}P_6$, resulting in (Si + P) contents

456   ranging from ~5.5 to ~7.0 per formula unit ($\square \approx$ 0-1.5, Fig. 4). Lower (Si + P) contents would be

457   expected because the EDX analyses on foil #6034 were done with a non-analytical TEM holder,

458   resulting in a small increase in the Ti signal. Consequently, we consider the crystallographic data

459   to be more compelling than the compositional data reported in Table 3 and in the literature.

460   **Kangjinlaite – a new compound of the $Ho_{11}Ge_{10}$ type**

461   Kangjinlaite is isostructural with synthetics of the $Ho_{11}Ge_{10}$ type, the structure of which was first

462 determined by Smith et al. (1967). In the 1960s – 1990s isostructural compounds ranging widely

463 in composition (37 elements in all, Fig. 9) were shown belong to this structure type. After it was

464 realized (e.g., Rauscher et al. 2007; Jeon et al. 2016) that compounds isostructural with $Ho_{11}Ge_{10}$

465 are potential thermoelectric material, syntheses of phases isostructural with $Ho_{11}Ge_{10}$ soared,

466 with over 30 compounds reported since 2012, although most of the new phases are versions of

467 known phases doped to improve their thermoelectric capability.

468

469 Despite there now being over 70 compounds containing 37 elements isostructural with $Ho_{11}Ge_{10}$,

470 our literature search has not revealed a report of the synthesis of an analogue of kangjinlaite in

471 the Ti-Si-P ternary system or in the Ti-P or Ti-Si binary systems. Moreover, none of the

472 compounds isostructural with $Ho_{11}Ge_{10}$ contain P even as a minor substituent at the Ge site, thus

473 kangjinlaite adds P as the 38th element to be found in the $Ho_{11}Ge_{10}$ structure type. Moreover,

474 only one isostructural compound contains As ($Eu_{11}As_{10}$, Taylor et al. 1978), suggesting but a

475 limited potential for a P-bearing analogue. In none of the reported compounds is Ti the dominant

476 cation at the Ho sites; in the two compounds containing Ti, Sc and Zr are the dominant cations

477 (Markiv et al. 1989). Several isostructural compounds contain Si, and in two of these, Si is

478 dominant at the sites occupied by Ge in the prototype, $Sc_7Cr_{4+x}Si_{10-x}$ [$x = 0.8$] (Kutar et al. 1985)

479 and $Sc_7Re_{4-x}Si_{10+x}$ [$x = 0.65$] (Zhao et al. 1988). These two compounds, together with an Mn-

480 bearing germanide, $Sc_7Mn_{4+x}Ge_{10-x}$ [$x = 1.3$] reported by Kutar et al. (1988), are the most

481 compact of the 70 synthetic phases for which crystallographic data are available (Table 5, Fig.

482 10) in terms of cell volume per formula unit and in terms of the Ti1-Ti3 bond length, a

483 representative vector that includes all three cell components. However, our data show that

484 kangjinlaite is even more compact, and thus the most compact of the phases isostructural with

485     $Ho_{11}Ge_{10}$.

486   **The ternary Ti-Si-P system.**

487

488   Badengzhuite, zhiqinite, kangjinlaite and wenjiite in foil #5358 are composed almost exclusively

489   of Ti, Si and P, with a maximum of 2 wt% V, 3 wt% Cr, 2 wt% Mn and 6 wt% Fe in the latter

490   two phases (Tables 1-3). Xu et al. (2018) described a spheroid with similar levels of impurities,

491   in which larger grains can be provisionally identified as wenjiite (61.3 wt% Ti, 18.5 wt% Si, 6.8

492   wt% P) and kangjinlaite (59.0 wt% Ti, 23.0 wt% Si, 8.4 wt% P). These grains are set in a matrix

493   provisionally identified as a mixture of zhiqinite and badengzhuite since both Si (37.9 wt.%) and

494   P (2.3 wt.%) are present. Their analyses also gave 2.1-4.4 wt% N and 3.0-5.7 wt% C, which

495   suggests admixture of osbornite and khamrabaevite with the Ti-Si-P phases in their spheroid.

496

497   Nonetheless, melts that crystallized to the two spheroids are closer to being a ternary Ti-P-Si

498   system than other aggregations of intermetallic phases, which presumably are also crystallized

499   melts in the Luobusa chromitite. For example, jingsuiite, osbornite, khamrabaevite, Fe-Ti

500   silicides and oxides are widespread constituents in such aggregations. A comparable chemical

501   complexity is reported for crystallized melts at Mount Carmel, including several containing

502   Ti_5Si_3, i.e., wenjiite (Griffin et al. 2021).

503

504   On the basis of the phase relationships in the Ti-Si-P ternary system, Xiong et al. (2020) inferred

505   that the 4 minerals in the spheroid crystallized with decreasing temperature in the sequence

506   wenjiite → kangjinlaite → zhiqinite + badengzhuite (Fig. 11). This interpretation is supported by

507   similarity with relationships reported in other binary systems containing intermetallic compounds

22

508 isostructural with Mn_5Si_3 and $Ho_{11}Ge_{10}$ (Fig. 12). For the 9 binaries involving Ge or Sn, the

509 Mn_5Si_3 analogue melts congruently in 8 cases, whereas the $Ho_{11}Ge_{10}$ analogue never does.

510 Instead the $Ho_{11}Ge_{10}$ analogue melts peritectically, generally to an Mn_5Si_3 analogue, and less

511 commonly to compounds with a 5:4 stoichiometry, which are listed in the column of intervening

512 phases in Figure 12. The 5 binaries involving Sb or Bi show a varied response: (1) compounds

513 having the $Ho_{11}Ge_{10}$ and Mn_5Si_3 type structures melt peritectically to an intervening phase, (2)

514 $Ca_{11}Sb_{10}$ melts congruently, while Ca_5Sb_3 melts peritectically, or (3) Sr_5Bi_3 inverts from a

515 Mn_5Si_3 type structure to a Yb_5Sb_3 type structure, and latter compound melts congruently. Since

516 we would expect the Ti-Si system to behave more like systems involving Ge or Sn than systems

517 involving Sb and Bi, we suggest that kangjinlaite melts peritectically to wenjiite and that the

518 upper temperature limit for end member kangjinlaite is less than 1920 °C (Fig. 11b). Moreover,

519 the Mn_5Si_3 type structure melts at a higher temperature than the $Ho_{11}Ge_{10}$ type structure in 13 of

520 the 14 systems (excluding Ti-Si), the exception being the Ca-Sb system, more evidence that the

521 Mn_5Si_3 type structure tends to form at higher temperatures than the $Ho_{11}Ge_{10}$ type structure.

522

523 Wenjiite would be expected to have crystallized at a lower temperature in the ternary system than

524 in the bounding binary systems (Xiong et al. 2020). Comparison with the impact of Fe on the Ti–

525 Si system (Weitzer et al. 2008) suggests that the impact of P on the Ti–Si system could be several

526 hundreds of degrees Celsius and thus final crystallization to zhiqinite + badengzhuite would be

527 well below the temperature of 1500 °C for the congruent melting of zhiqinite (Fig. 11), i.e. in the

528 range of ~1100 – 1300 °C, temperatures plausible for the upper mantle.

529

530 The presence of kangjinlaite in the natural ternary system distinguishes it from the two bounding

23

531 synthetic binary systems Ti-P and Ti-Si, neither of which includes a compound isostructural with

532 $Ho_{11}Ge_{10}$. Conversely, the synthetic phases intermediate in Ti/Si and Ti/P ratio, i.e., Ti_5Si_4, TiSi

533 and Ti_4P_3, have yet to be confirmed in a natural system. Griffin et al. (2021) did report 9 analyses

534 of isolated Fe-bearing Ti-Si inclusions in corundum with a stoichiometry close to Ti_5Si_4, but did

535 not provide the crystallographic data needed to identify the inclusions. The different assemblages

536 could simply reflect (1) influence of minor constituents, (2) activities of H and O in a gaseous

537 phase associated with the intermetallics, or (3) P and Si interacting with one another in a way to

538 foster crystallization of P-bearing kangjinlaite at the expense of P-Si-bearing phases isostructural

539 with Ti_5Si_4, TiSi or Ti_4P_3. Alternatively, it is not inconceivable that pressure above atmospheric

540 played a role by favoring kangjinlaite over the other phases. Pressures of 20-30 kbar have been

541 estimated for crystallization of the melts (Xiong et al. 2020, 2022), whereas relationships in the

542 bounding binaries were determined by syntheses at atmospheric pressure, and as far as we are

543 aware, syntheses of these phases at elevated pressures have not yet been attempted except for

544 $TiSi_2$ (to 520 kbar, Li et al. 2013). Kangjinlaite is more compact than other phases isostructural

545 with $Ho_{11}Ge_{10}$ (Fig. 10). It has been noted that room-pressure germanate crystal chemistry could

546 serve as a guide for high-pressure silicate crystal chemistry (Finger and Hazen 2000), but

547 whether room pressure germanide crystal chemistry could serve the same function for silicide

548 crystal chemistry has not been previously considered, as far as we are aware.

549

550 **Implications**

551 As we noted in the section describing the method of sample preparation, the question whether the

552 highly reduced phases in the Luobusa ophiolite are natural or the result of technogenic

553 contamination remains highly controversial (e.g., Litasov et al. 2019a,b). While we regard

554 wenjiite and kangjinlaite to be natural minerals, fortunately there are implications of this study

24

555   that have significant relevance to materials science even if these phases were someday to be

556   shown to be technogenic. Wenjiite has implications for understanding polymorphism in

557   intermetallic compounds. It is isostructural with a large number of compounds (>175, Corbett

558   2000), but this structure type is only one of four principal types reported for the 5:3

559   stoichiometry (Franceschi and Ricaldone 1984). Two structure types have been reported in 11

560   binary systems, one is isostructural with wenjiite, the other isostructural with one or both of two

561   closely related orthorhombic phases isostructural with Yb_5Sb_3 or Y_5Bi_3 (Grew 2021). However,

562   evidence for which polymorph forms at higher temperatures in these systems is contradictory.

563   One might speculate that since compounds isostructural with wenjiite melt congruently and at

564   the highest temperature in 8 of 9 of the binary systems most closely related to Ti-Si (Fig. 12), it

565   is likely that such compounds form from the orthorhombic compounds with increasing

566   temperature.

567

568   The occurrence of wenjiite also raises the question why is polymorphism restricted to relatively

569   few systems, while in other systems only one polymorph has been reported (Grew 2021). In

570   relating radius ratio, cell volume and electronegativity for intermetallic compounds having 5:3

571   stoichiometry, Bruzzone et al. (1978) and Franceschi and Ricaldone (1984) attempted to explain

572   the distribution of structures of these compounds.

573

574   We have demonstrated that wenjiite and kangjinlaite, followed by badengzhuite and zhiqinite,

575   are the result of crystallization of a ternary Ti-Si-P melt during cooling. To our knowledge, this

576   represents an "experiment" that has not yet been carried out in the laboratory. As far as we are

577   aware, neither mineralogists nor material scientists appear to have previously investigated this

25

578   system. The "experiment" has yielded a phase new to science – kangjinlaite, which has not been

579   previously reported either in nature or as a product of synthesis. Moreover, like other compounds

580   isostructural with $Ho_{11}Ge_{10}$, kangjinlaite could have potential technological applications. Its

581   presence in the Luobusa corundum also raises the question of why such a compound has not yet

582   been synthesized in the laboratory, given the numerous studies in recent decades on the Ti-Si and

583   Ti-P binary systems.

584

585   Discovering and characterizing kangjinlaite and wenjiite, as well as zhiqinite ($TiSi_2$) and

586   badengzhuite (TiP) (Xiong et al. 2020), was only possible thanks to the recently developed 3-

587   dimensional electron diffraction technique. The four minerals, together with a dmisteinbergite-

588   like mineral now under study, occur together in an area of less than 100 μm^2. The new technique

589   enables the collection of structural data suitable for ab-initio solution and refinement of crystal

590   structures from single grains of less than 1 μm in size in situ, obviating the need to extract tiny

591   grains from a polyphasic solid matrix. The possibility to perform single-crystal-like analysis at

592   this scale opens unprecedented opportunities not only for mineralogy and petrology at the nano-

593   scale, for example, nano-scale melt inclusions, but also for materials science, since tiny droplets

594   of crystallized intermetallic melts can be readily investigated.

595

610

611   **References**

612   Achgar, K., Kardellass, S., Selhaoui, N. and Bouirden, L. (2017) Thermodynamic optimization

613   of the erbium–germanium binary system. Journal of Alloys and Compounds, 724, 1157-

614   1166.

615   Achgar, K., Iddaoudi, A., Tamim, R., Azza, H.and Bouirden, L. (2018a) Thermodynamic

616   evaluation of the germanium-lutetium and dysprosium-germanium binary systems.

617   Calphad, 62, 18-29.

618   Achgar, K., Kardellass, S., Azza, H. and Selhaoui, N. (2018b) Thermodynamic evaluation of the

619   thulium–germanium binary system. Journal of Thermal Analysis and Calorimetry, 131,

620   2699–2707.

621   Achgar, K., Kardellass, S. and Selhaoui, N. (2018c) Thermodynamic assessment of the

622   ytterbium–germanium binary system. Journal of Thermal Analysis and Calorimetry,131,

623   443–453.

624   Ballhaus, C., Wirth, R., Fonseca, R.O.C., Blanchard, H., Pröll, W., Bragagni, A., Nagel, T.,

625   Schreiber, A., Dittrich, S., Thome, V., Hezel, D.C., Below, R., Cieszynski, H. (2017)

626   Ultra-high pressure and ultra-reduced minerals in ophiolites may form by lightning

627   strikes. Geochemical Perspectives Letters 5, 42-46.

628   Ballhaus, C., Fonseca, R.O.C., Bragagni, A. (2018) Reply to Comment on "Ultra-high pressure

629   and ultra-reduced minerals in ophiolites may form by lightning strikes" by Griffin et al.,

630   2018: No evidence for transition zone metamorphism in the Luobusa ophiolite.

631   Geochemical Perspectives Letters, 7, 3-4.

632   Ballhaus, C., Helmy, H.M., Fonseca, R.O.C., Wirth, R., Schreiber, A., l, Jöns, N. (2021) Ultra-

633   reduced minerals in ophiolites cannot come from Earth's mantle. American Mineralogist,

634   106, in press.

635   Bärnighausen, H., Knausenberger, M., Brauer, G. (1965) Die Kristallstruktur von $TiP_{0.63}$. Acta

636   Crystallographica, 19, 1-5.

637   Bilibrov, Y.M., Trachevskii, V.V., Bondar, A.A., Velikanova, T.Y., Artyukh, L.V., Pashchenko,

638   V.Y., Soboliev, V.B. (2014) Boron solubility in silicide Ti_5Si_3. Journal of Phase

639   Equilibria and Diffusion, 35, 406-412.

640   Bruzzone, G., Franceschi, E. and Merlo, F. (1978) Intermediate phases formed by Ca, Sr and Ba,

641   Journal of the Less-Common Metals, 60, 59 – 63.

642   Burla, MC, Caliandro, R., Carrozzini, B; Cascarano, GL; Cuocci, C; Giacovazzo, C; Mallamo,

643   M; Mazzone, A; Polidori, G. (2015) Crystal structure determination and refinement via

644   SIR2014. Journal of Applied Crystallography, 48, 306-309. DOI:

645   10.1107/S1600576715001132

646   Cliff, G., and Lorimer, G.W. (1975). The quantitative analysis of thin specimens. Journal of

647   Microscopy, 103, 203-207.

648   Corbett, J.D. (2000) Exploratory Synthesis in the solid state. Endless Wonders. Inorganic

649   Chemistry, 39, 5178-5191

650   Corbett, J.D and León-Escamilla, E.-A. (2003) Role of hydrogen in stabilizing new hydride

651   phases or altering old ones, Journal of Alloys and Compounds, 356–357, 59–64

652   Corbett, J.D., Garcia, E., Guloy, A.M., Hurng, W.-M., Kwon, Y.-U., León-Escamilla, E. (1998)

653   Widespread interstitial chemistry of Mn_5Si_3-type and related phases. Hidden impurities

654   and opportunities. Chem. Mater., 10, 2824-2836

655   Dobrzhinetskaya, L.F., Wirth, R., Yang, J., Green, H.W., Hutcheon, I.D., Weber, P.K. and Grew,

656   E.S. (2014) Qingsongite, natural cubic boron nitride: The first boron mineral from the

657   Earth's mantle. American Mineralogist, 99, 764-772.

658 Eremenko, V.N., Obushenko, I.M., Buyanov, Yu.I. (1980) Phase-diagram for the holmium-

659   germanium system. Dopovidi Akademiïa Nauk Ukraïn'skoï RSR, Seriia Heolohichni

660   chimichni ta biolohechi Nauku, 7, 87-91 (in Ukrainian).

661 Eremenko, V.N., Meleshevich, K.A., Buyanov, Yu.I. and Martsenyuk, P.S. (1988) Phase diagram

662   of the terbium-germanium system. Ukrainskii Khimicheskii Zhurnal, 54(10), 1019-1023.

663 Essene, E. J., and Fisher, D.C. (1986) Lightning strike fusion: Extreme reduction and metal-

664   silicate liquid immiscibility. Science, 234, 189-193

665   https://doi.org/10.1126/science.234.4773.189.

666 Fang Q, Bai W, Yang J, Rong H, Shi N, Li G, Xiong M, Ma Z (2013) Titanium, Ti, a new

667   mineral species from Luobusha, Tibet, China. Acta Geologica Sinica 87, 1275-1280.

668 Finger, L.W. and Hazen, R.M. (2000) Systematics of high-pressure silicate structures. Reviews

669   in Mineralogy and Geochemistry, 41, 123-156.

670 Fiore, M., Neto, F.B., de Farias Azevedo, C.R. (2016) Assessment of the Ti-rich corner of the Ti-

671   Si phase diagram: The recent dispute about the eutectoid reaction. Materials Research,

672   19(4), 942-953.

673 Franceschi, E.A. and Ricaldone, F. (1984) Intermetallic binary phases of 5:3 composition, Revue

674   de Chimie Minérale, 1984, 21, 202-220

675 Frommeyer, G. and Rosenkranz, R. (2004) Structures and properties of the refractory silicides

676   Ti_5Si_3 and $TiSi_2$ and Ti-Si-(Al) eutectic alloys. In: Senkov, O.N.; Miracle, D.B.; Firstov,

677   S.A. Metallic Materials with High Structural Efficiency, NATO Science Series, Series II:

678   Mathematics, Physics and Chemistry, 146, 287-308.

679   Gemmi, M., Mugnaioli, E., Gorelik, T.., Kolb, U., Palatinus, L., Boullay, P., Hovmöller, S.,

680   Abrahams, P.A. (2019) 3D Electron Diffraction: The nanocrystallography revolution.

681   ACS Central Science, 2019, 5, 1315−1329.

682   Grew, E.S. (2021) Polymorphism in the Sr-Bi System. Journal of Phase Equilibria and Diffusion.

683   https://doi.org/10.1007/s11669-021-00925-6.

684   Griffin, W.L., Gain, S.E. M., Saunders, M., Bindi, L., Alard, O., Toledo, V., O'Reilly, S.Y.

685   (2020) Parageneses of TiB_2 in corundum xenoliths from Mt Carmel, Israel: Siderophile

686   behaviour of boron under reducing conditions. American Mineralogist, 105, 1609–1621.

687   Griffin, W.L., Gain, S.E. M., Saunders, M.J., Huang, X.J., Alard, O., Toledo, V., O'Reilly, S.Y.

688   (2021) Immiscible metallic melts in the upper mantle beneath Mount Carmel, Israel:

689   Silicides, phosphides and carbides. American Mineralogist, 106, in press.

690   Hahn, H. and Ness, P. (1957) Zur Frage der Existenz von Subchalkogenidphasen des Titans.

691   Naturwissenschaften, 44, 581.

692   Iddaoudi, A., Selhaoui, N., Ait Amar, M., Kardellass, S. and Bouirden, L. (2013)

693   Thermodynamic reassessment of the Sn–Y system. Journal of Optoelectronics and

694   Advanced Materials, 15, 1280 – 1285.

695   Jeon, B.-Y., Nam, G., Lee, D.W., Ok, K.M., You, T.-S. (2016) $Ce_{11}Ge_{3.73(2)}In_{6.27}$: Solid-state

696   synthesis, crystal structure and site-preference. Journal of Solid State Chemistry, 236,

697   195–202.

698   Kolb, U., Gorelik, T., Kübel, C., Otten, M.T., Hubert, C. (2007) Towards automated diffraction

699   tomography: Part I—Data acquisition. Ultramicroscopy, 107, 507-513.

700   doi.org/10.1016/j.ultramic.2006.10.007

701   Kolb U., Mugnaioli E., Gorelik T.E. (2011) Automated electron diffraction tomography - A new

702   tool for nano crystal structure analysis. Crystal Research and Technology, vol. 46, (no. 6),

703   pp. 542-554 https://doi.org/10.1002/crat.201100036

704   Krikorian, O.H. (1955) High temperature studies: I. Reactions of the Refractory Silicides with

705   Carbon and with Nitrogen. II. Thermodynamic Properties of the Carbides. III. Heat of

706   Formation of the $^3\pi_u$ State of C_2 from Graphite. |Lawrence Berkeley National Radiation

707   Laboratory. Ph.D. Thesis.

708   Kutar, B.Ya., Bodak, O.I., Zavodnik, V.E. (1985) The silicide $Sc_7Cr_{4+x}Si_{10-x}$ ($x = 0.8$): the first

709   representative of a superlattice structure of the $Ho_{11}Ge_{10}$ type. Soviet Physics

710   Crystallography, 30(5), 521-523 (translation of Kristallografia, 30, 899-903, 1985).

711   Kutar, B.Ya., Andrusyak, R.I. and Zavodnik, V.E. (1988) The germanides $Sc_7Mn_{4+x}Ge_{10-x}$ ($x =$

712   1.3) and $Sc_7Cr_{4+x}Ge_{10-x}$ ─new representatives of compounds with superstructure of the

713        $Ho_{11}Ge_{10}$ type. Soviet Physics Crystallography, 33(1), 141-142 (translation of

714   Kristallografia, 33, 240-241, 1988).

715   León-Escamilla, E.A. and Corbett, J.D. (2006) Hydrogen in polar intermetallics. Binary pnictides

716   of divalent metals with Mn_5Si_3-type structures and their isotypic ternary hydride

717   solutions, Chemical Materials, 18, 4782-4792.

718   Li, C.Y., Yu, Z.H., Liu, H.Z., and Lü, T.Q.: The crystallographic stability and anisotropic

719   compressibility of C54- type $TiSi_2$ under high pressure. Journal of Physics and Chemistry

720   of Solids, 74, 1291–1294, https://doi.org/10.1016/j.jpcs.2013.04.006, 2013.

721   Litasov, K. D., Kagi, H. Bekker, T. B. (2019a) Enigmatic super-reduced phases in corundum

722   from natural rocks: Possible contamination from artificial abrasive materials or

723   metallurgical slags. Lithos 340–341 (2019) 181–190.

724 Litasov, K. D., Bekker, T. B. Kagi, H. (2019b) Discussion. Reply to the discussion of "Enigmatic

725   super-reduced phases in corundum from natural rocks: Possible contamination from

726   artificial abrasive materials or metallurgical slags" by Litasov et al. (Lithos, v.340–341,

727   p.181–190) by W.L. Griffin, V. Toledo and S.Y. O'Reilly. Lithos 340–341 (2019) 181–

728   190. Lithos, 348. DOI: 10.1016/j.lithos.2019.105170

729 Lu, N., Wang, J. (2018) Odd aromatic Si4 ring stabilized by V–V bond passing through it: May

730   π-bonding form without σ-bonding as precondition? International Journal of Quantum

731   Chemistry, 118, e25788

732 Lundström, T. and Snell, P.-O. (1967) Studies of crystal structures and phase relations in the Ti-

733   P system. Acta Chemica Scandinavica, 21, 1343-1352.

734 Markiv, V., Belyavina, N.N. and Kazachkova, S.S. (1989) Crystal structure of Sc_5Ga_4 and new

735   compounds of the structural type $Ho_{11}Ge_{10}$. Russian Metallurgy, 1989(3), 191-194.

736 Momma, K.; Izumi, F. (2011) VESTA 3 for three-dimensional visualization of crystal, volumetric

737   and morphology data. Journal of Applied Crystallography, 44, 1272–1276.

738 Mugnaioli E., Gemmi M. (2018) Single-crystal analysis of nanodomains by electron diffraction

739   tomography: Mineralogy at the order-disorder borderline. Zeitschrift für Kristallographie

740   - Crystalline Materials, 233, 163-178.

741 Mugnaioli E., Gorelik T., Kolb U. (2009)"Ab initio" structure solution from electron diffraction

742   data obtained by a combination of automated diffraction tomography and precession

743   technique. *Ultramicroscopy*, vol. 109, (no. 6), pp. 758-765. doi:

744   10.1016/j.ultramic.2009.01.011

745   Mugnaioli, E., Bonaccorsi, E., Lanza, A.E., Elkaim, E., Diez-Gómez, V., Sobrados, I., Gemmi,

746   M., Gregorkiewitz, M. (2020a) The structure of kaliophilite KAlSiO$_4$, a long-lasting

747   crystallographic problem. IUCrJ, 7, 1070–1083.

748   Mugnaioli, E., Lanza, A.E., Bortolozzi, G., Righi, L., Merlini, M., Cappello, V., Marini, L.,

749   Athanassiou, A. Gemmi, M. (2020b) Electron Diffraction on Flash-Frozen Cowlesite

750   Reveals the Structure of the First Two-Dimensional Natural Zeolite. ACS Central

751   Science, 6, 1578−1586.

752   Nederlof, I.; van Genderen, E.; Li, Y.-W.; Abrahams, J.P. (2013) A Medipix quantum area

753   detector allows rotation electron diffraction data collection from submicrometre three-

754   dimensional protein crystals. Acta Crystallographica D, 69, 1223–1230.

755   Nowotny, H., Auer-Welsbach, H., Bruss, J., Kohl, A. (1959) Ein Beitrag zur Mn$_5$Si$_3$-Struktur

756   (D8$_8$-Typ). Monatshefte für Chemie, 90, 15-23

757   Okamoto, H. (2007) P-Ti (Phosphorus-titanium). Journal of Phase Equilibria and Diffusion, 28,

758   587.

759   Okamoto, H. (2013a) Supplemental literature review of binary phase diagrams: Ag-Ni, Al-Cu,

760   Al-Sc, C-Cr, Cr-Ir, Cu-Sc, Eu-Pb, H-V, Hf-Sn, Lu-Pb, Sb-Yb, and Sn-Y. Journal of

761   Phase Equilibria and Diffusion, 34, 493–505.

762   Okamoto, H. (2013b) Eu-Sb (europium-antimony). Journal of Phase Equilibria and Diffusion,

763   34, 146-147.

764   Okamoto, H. (2014) Supplemental literature review of binary phase diagrams: Al-Br, B-Cd, Cd-

765   Mg, Cd-Ti, Er-Fe, Fe-Nd, Ge-Na, Ge-Ni, Ge-Sc, Hf-W, Pb-Yb, and Re-Ti. Journal of

766   Phase Equilibria and Diffusion, 35, 195–207.

767 Okamoto, H. (2015) Supplemental literature review of binary phase diagrams: B-La, B-Zn, Bi-

768 La, Bi-Ti, Cd-Pr, Ce-Ga, Cu-Na, Ge-Ta, Ge-Y, H-Zr, Na-Si, and Pb-Sc. Journal of Phase

769 Equilibria and Diffusion, 36:644–655.

770 Okamoto, H. (2016) Supplemental literature review of binary phase diagrams: Al-Nd, Al-Sm,

771 Al-V, Bi-Yb, Ca-In, Ca-Sb, Cr- Nb, Cu-Ga, Ge-O, Pt-Sn, Re-Y, and Te-Yb. Journal of

772 Phase Equilibria and Diffusion, 37, 350–362.

773 Palatinus, L.; Corrêa C. A., Steciuk G., Jacob D., Roussel P., Boullay P., Klementová M., Gemmi

774 M., Kopeček J. Domeneghetti M. C., Cámara F.; Petříček V. (2015a) Structure refinement

775 using precession electron diffraction tomography and dynamical diffraction: tests on

776 experimental data. Acta Crystallographica B, 71, 740–751.

777 Palatinus, L.; Petříček, V.; Corrêa, C. A. (2015b) Structure refinement using precession electron

778 diffraction tomography and dynamical diffraction: theory and implementation. Acta

779 Crystallographica A , 71, 235-244.

780 Palatinus, L.; Brázda, P., Jelínek, M., Hrdá, J., Steciuk G., Klementova M. (2019) Specifics of

781 the data processing of precession electron diffraction tomography data and their

782 implementation in the program *PETS2.0*. Acta Crystallographica B, 75, 512–522.

783 Petříček, V., Dušek, M. and Palatinus, L. (2014) Crystallographic computing system JANA2006:

784 general features. Zeitschrift für Kristallographie, 229, 345–352.

785 Pietrokowsky, P. and Duwez, P. (1951) Crystal structure of Ti_5Si_3, Ti_5Ge_3 and Ti_5Sn_3. Journal of

786 Metals, 3, 772-773

787 Rauscher, J.F., Kauzlarich, S.M., Ikeda, T. and G. J. Snyder,G.J. (2007) Synthesis, structure, and

788 high temperature thermoelectric properties of $Yb_{11}Sb_{9.3}Ge_{0.5}$. Zeitschrift für Anorganische

789 und Allgemeine Chemie, 633, 1587-1594.

790   Smith, G.S., Johnson, Q. and Tharp, A.G. (1967) The crystal structure of $Ho_{11}Ge_{10}$. Acta

791   Crystallographica, 23, 640-644.

792   Steciuk, G., Ghazisaeed, S., Kiefer, B., Plášil, J. (2019a) Crystal structure of vyacheslavite,

793        $U(PO_4)(OH)$, solved from natural nanocrystal: a precession electron diffraction

794   tomography (PEDT) study and DFT calculations. RSC Advances, 9, 19657–19661.

795   Steciuk, G., Palatinus, L., Rohlíček, J., Ouhenia, S., Chateigner, D. (2019b) Stacking sequence

796   variations in vaterite resolved by precession electron diffraction tomography using a

797   unified superspace model. Scientific Reports, 9, 9156.

798   Svechnikov, V.N., Kocherzhinskiy, Yu.A., Yubko, L.M., Kulik, O.G., Shishkin, Ye. A. (1970)

799   Phase Diagram of the Titanium-Silicon System. Doklady Akademii Nauk SSSR,

800   193(2):393-396 (in Russian).

801   Taylor, J.B., Calvert, L.D., Utsunomiya, T., Wang, Y. and Despault, J.G. (1978) Rare earth

802   arsenides: The metal-rich europium arsenides. Journal of the Less-Common Metals, 57,

803   39 - 51

804   Thom, A.J., Young, V.G., Akinc, M. (2000) Lattice trends in $Ti_5Si_3Z_x$ (Z=B,C,N,O and $0 < x < 1$).

805   Journal of Alloys and Compounds, 296, 59–66.

806   Vincent, R. and Midgley, P.A. (1994) Double conical beam-rocking system for measurement of

807   integrated electron diffraction intensities. Ultramicroscopy 53, 271-282.

808   Wang, Y., Xin, J., C hen, C., Liu, S., Hu, B. and Du, Y. (2014) Thermodynamic assessment of

809   the Sr–In and Sr–Bi systems supported by first-principles calculations. CALPHAD:

810   Computer Coupling of Phase Diagrams and Thermochemistry, 45, 49–54.

811   Wang, Y. L. Calvert, D., Gabe, E.J. and Taylor, J.B. (1978) Structure of two forms of europium

812   arsenide Eu_5As_3. Acta Crystallographica, B34, 2281-2284.

813   Weitzer, F., Schuster, J.C., Naka, M., Stein, F., Pulm, M. (2008) On the reaction scheme and

814   liquidus surface in the ternary system Fe—Si—Ti. Intermetallics, 16, 273—282

815   Williams, J.J., Kramer, M.J., Akinc, M., Malik, S.K. (2000a) Effects of interstitial additions on

816   the structure of Ti_5Si_3. J. Materials Research, 15, 1773-1779.

817   Williams, J.J., Ye., Y.Y., Kramer, M.J., Ho, K.M., Hong, L., Fu, C.L. Malik, S.K. (2000b)

818   Theoretical calculations and experimental measurements of the structure of Ti_5Si_3 with

819   interstitial additions. Intermetallics, 8, 937-943.

820   Wirth, R., 2004. Focused ion beam (FIB): a novel technology for advanced application of micro-

821   and nanoanalysis in geosciences and applied mineralogy. European Journal of

822   Mineralogy **16**, 863–877.

823   Wirth, R., 2009. Focused ion beam (FIB) combined with SEM and TEM: advanced analytical

824   tools for studies of chemical composition, microstructure and crystal structure in

825   geomaterials on a nanometre scale. Chemical Geology **261**, 217–229.

826   Wolf, S., Klopper, W., Feldmann, C. (2013) Ge12{Fe(CO)3}8(μ-I)4: a germanium–iron cluster

827   with Ge4, Ge2 and Ge units. Chemical Communications, 54, 1217.

828   Xiong, F., Xu, X., Mugnaioli, E., Gemmi, M., Wirth, R., Grew, E.S. Robinson, P.T., Yang, J.

829   (2020) Badengzhuite, TiP, and zhiqinite, $TiSi_2$, two new minerals from the Cr-11

830   chromitite orebody, Luobusa ophiolite, Tibet, China: Evidence for super-reduced mantle-

831   derived fluids? European Journal of Mineralogy, 32, 557–574.

832   Xiong, F., Xu, X., Mugnaioli, E., Gemmi, M., Wirth, R., Yang, Y., and Grew, E. S.(2021a)

833   Wenjiite, IMA 2019-107c, in: CNMNC Newsletter 61, Eur. J. Mineral., 33,

834   https://doi.org/10.5194/ejm-33-299-2021, 2021.

835   Xiong, F., Xu, X., Mugnaioli, E., Gemmi, M., Wirth, R., Grew, E. S., and Yang, Y.(2021b)

836   Kangjinlaite, IMA 2019-112b, in: CNMNC Newsletter 61, Eur. J. Mineral., 33,

837   https://doi.org/10.5194/ejm-33-299-2021, 2021.

838   Xiong, F., Xu, X., Mugnaioli, E., Gemmi, M., Wirth, R., Grew, E.S. and Robinson, P.T. (2022)

839   Jingsuiite, TiB_2, a new mineral from the Cr-11 podiform chromitite orebody, Luobusa

840   ophiolite, Tibet, China: Implications for recycling of boron. American Mineralogist (in

841   press).

842   Xu, X., Yang, J., Chen, S., Fang, Q. and Bai, W. (2009) Unusual Mantle Mineral Group from

843   Chromitite Orebody Cr-11 in Luobusa Ophiolite of Yarlung-Zangbo Suture Zone, Tibet.

844   *Journal of Earth Science,* **20,** 284–302.

845   Xu, X.Z., Yang, J.S., Robinson, P.T., Xiong, F.H., Ba, D.Z., Guo, G.L. (2015) Origin of

846   ultrahigh pressure and highly reduced minerals in podiform chromitites and associated

847   mantle peridotites of the Luobusa ophiolite, Tibet. *Gondwana Research* 27, 686–700

848   Xu, X.Z., Yang, J.S., Xiong, F.H., Guo, G.L. (2018) Characteristics of titanium-bearing

849   inclusions found in corundum of Luobusa podiform chromitite, Tibet. *Earth Science,*

850   43(4), 1025-1037 (in Chinese with English abstract).

851   Yu, Z. (1984) Two new minerals gupeiite and xifengite in cosmic dusts from Yanshan, Acta

852   Petrologica Mineralogica et Analytica 3, 231-238 (in Chinese with an English abstract)

853   Yusupov R. G., Stanley, C. J., Welch, M. D., Spratt, J., Cressey, G., Rumsey, M. S., Seltmann,

854   R. and Igamberdiev, E. (2009) Mavlyanovite, Mn_5Si_3: a new mineral species from a

855   lamproite diatreme, Chatkal Ridge, Uzbekistan. Mineralogical Magazine, 73, 43-50.

856   Zaitsev, A.I., Sheikova, N.E. and Mogutnov, B.M. (1997) Thermodynamic properties and phase

857   equilibria in the Ca-Sb system. Zeitschrift für Metallkunde, 88, 250-255.

858   Zhao, J.T., Chabot, B. and Parthé, E. (1988) $Sc_7Re_4Si_{10}$, a ternary substitution variant of the

859   tetragonal $Ho_{11}Ge_{10}$ type. Acta Crystallographica, C44, 397-399

860

861   **TABLES**

862   Table 1. Chemical data for wenjiite in foil #5358 (open squares in Figure 1)

	Foil #	5358	5358	5358	5358	Average
863						
864	Analysis	416	433	C31	C32	(Stdev)
865	Date[1]	2019-06-18	2019-06-27	2019-12-18	2019-12-18	
866	3D ED[2]	YES	YES	—	—	—
867		Net counts				
868	C	0	0	0	0	—
869	O	49	36	38	25	—
870	Si	601	493	339	139	—
871	P	147	159	87	41	—
872	Ti	1605	1272	859	417	—
873	V	41	11	22	6	—
874	Cr	44	52	18	15	—
875	Mn	41	17	2	3	—
876	Fe	31	27	18	0	—
877	Cu[3]	582	729	543	469	—
878						
879		wt% (1 sigma error)				
880	Si	21.65(0.93)	21.96(1.03)	22.88(1.29)	20.17(1.77)	21.67(1.13)
881	P	5.41(0.52)	7.27(0.66)	6.07(0.72)	6.22(1.04)	6.24(0.77)
882	Ti	65.84(2.67)	64.53(2.76)	65.99(3.14)	69.19(4.19)	66.39(1.98)
883	V	1.76(0.32)	0.72(0.23)	1.83(0.44)	1.18(0.51)	1.37(0.52)
884	Cr	1.94(0.34)	2.76(0.45)	1.49(0.40)	2.61(0.75)	2.20(0.59)
885	Mn	1.91(0.35)	1.12(0.30)	0.20(0.17)	0.64(0.40)	0.97(0.73)
886	Fe	1.49(0.31)	1.63 (0.36)	1.55(0.43)	0(0)	1.17(0.78)
887						
888		Atomic%				
889	Si	31.41	31.51	32.79	29.32	31.26(1.44)
890	P	7.12	9.46	7.88	8.20	8.17(0.97)
891	Ti	56.04	54.32	55.47	59.01	56.21(0.20)
892	V	1.40	0.57	1.44	0.95	1.09(0.41)
893	Cr	1.52	2.14	1.15	2.05	1.72(0.47)
894	Mn	1.42	0.82	0.15	0.48	0.72(0.54)
895	Fe	1.08	1.18	1.11	0	0.84(0.56)
896						
897	X_P	0.185	0.231	0.194	0.194	0.207(0.021)

898   Note: 1. Year-month-day. 2. 3D ED = 3-dimensional electron diffraction. 3. The Cu counts are
899   from the prong to which the foil is attached in the focused ion beam support grid. X_P = P/(P +
900   Si) atomic.

901
902

40

903

904   Table 2. Chemical data for kangjinlaite in foil #5358

Area	1	2	1	2	Average
Analysis no. (Fig. 1)	415	432	C-29	C-30	(stdev)
Date[1]	2019-06-18	2019-06-27	2019-12-18	2019-12-18	—
			Net counts		
C	0	0	0	0	—
O	4	37	0	2	—
Si	853	977	825	648	—
P	300	366	319	233	—
Ti	2032	2023	1841	1249	—
V	0	20	3	0	—
Cr	22	20	18	16	—
Mn	11	20	9	1	—
Fe	35	20	19	13	—
Cu[2]	321	587	489	372	—
			wt% (1 sigma error)		
Si	23.93(0.86)	25.92(0.87)	24.85(0.91)	27.55(1.13)	25.56(1.55)
P	8.66(0.60)	9.96(0.64)	9.89(0.67)	10.20(0.78)	9.68(0.69)
Ti	64.83(2.50)	61.04(2.36)	63.07(2.48)	60.47(2.60)	62.35(1.99)
V	0	0.72(0.19)	0.12(0.10)	0	0.21(0.34)
Cr	0.85(0.21)	0.77(0.19)	0.75(0.20)	0.94(0.26)	0.83(0.09)
Mn	0.45(0.16)	0.78(0.20)	0.40(0.16)	0.06(0.09)	0.42(0.29)
Fe	1.28(0.26)	0.81(0.21)	0.92(0.23)	0.78(0.25)	0.95(0.23)
			atomic %		
Si	33.63	35.81	34.53	37.64	35.40(1.74)
P	11.04	12.48	12.47	12.63	12.16(0.75)
Ti	53.45	49.47	51.42	48.46	50.70(2.21)
V	0	0.55	0.09	0	0.16(0.26)
Cr	0.65	0.57	0.56	0.69	0.62(0.06)
Mn	0.33	0.55	0.28	0.04	0.30(0.21)
Fe	0.91	0.56	0.64	0.53	0.66(0.17)
Total	100.01	99.99	99.99	99.99	100.00
X_{P}	0.247	0.258	0.265	0.251	0.256(0.008)

940   Note: [1]Year-month-day. [2]The Cu counts are from the prong to which the foil is attached in the
941   focused ion beam support grid. $X_P = P/(P + Si)$.

942

943 Table 3 Chemical data for wenjiite in foil #6034 (open rectangles in Figure 6)

Foil #	6034	6034	6034	6034	Average
Analysis	C45	C46	C47	C48	(Stdev)
Date[1]	2019-12-18	2019-12-18	2019-12-18	2019-12-18	
3D ED[2]	—	YES	—	—	
	Net counts				
C	0	0	0	0	—
O	32	13	12	45	—
Si	1257	929	1136	871	—
P	690	558	713	441	—
Ti	4479	3454	4122	3133	—
V	14	0	0	0	—
Cr	142	114	118	114	—
Mn	5	15	38	18	—
Fe	292	213	280	232	—
Cu[3]	1185	904	1118	801	—
	wt% (1 sigma error)				
Si	16.42(0.50)	15.81(0.55)	15.92(0.51)	16.24(0.59)	16.10(0.28)
P	9.29(0.48)	9.76(0.54)	10.29(0.53)	8.47(0.51)	9.45(0.77)
Ti	66.60(2.29)	66.86(2.37)	65.76(2.28)	66.45(2.39)	66.42(0.47)
V	0.27(0.09)	0	0	0	0.07(0.14)
Cr	2.25(0.24)	2.34(0.27)	2.01(0.23)	2.59(0.29)	2.30(0.24)
Mn	0.10(0.07)	0.38(0.12)	0.80(0.16)	0.49(0.14)	0.44(0.29)
Fe	5.09(0.38)	4.85(0.41)	5.22(0.39)	5.75(0.46)	5.23(0.38)
	Atomic%				
Si	24.19	23.32	23.43	24.08	23.76(0.44)
P	12.41	13.06	13.73	11.39	12.65(1.00)
Ti	57.56	57.87	56.77	57.80	57.50(0.50)
V	0.22	0	0	0	0.06(0.11)
Cr	1.79	1.87	1.60	2.08	1.84(0.20)
Mn	0.07	0.28	0.61	0.37	0.33(0.22)
Fe	3.77	3.60	3.86	4.29	3.88(0.29)
X_P	0.339	0.359	0.369	0.321	0.347(0.021)

Note: [1]Year-month-day. [2]3D ED = 3-dimensional electron diffraction. [3]The Cu counts are from the prong to which the foil is attached in the focused ion beam support grid. X_P = P/(P + Si)

982 Table 4. Coordinates and equivalent displacement parameters (U_{iso} Å^2) of atoms in wenjiite

Label	Williams[1]	x/a	y/b	z/c	U_{iso}	occupancy	multiplicity
Ti1	Ti^{4d}	⅔	⅓	0	0.0053(8)	1	4
Ti2	Ti^{6g}	0.7614(3)	0	0.25	0.0060(7)	1	6
Si1	Si	0.5981(6)	0.5981(6)	0.25	0.0071(9)	0.77	6
P1	—	0.5981(6)	0.5981(6)	0.25	0.0071(9)	0.23	6
Si2	Z	0	0	0	0.020(4)	0.385	2
P2	—	0	0	0	0.020(4)	0.115	2

990 Note: 1. Site designation from Williams et al. (2000a,b)

991

992

Table 5. Bond lengths in wenjiite and in synthetic analogs (in Å)

Bonds	$Ti_{10}(Si,P,\square)_7$ wenjiite	Ti_5Si_3 synthetic	Ti_5P_{3+x} synthetic
Source	(1)	(2)	(3)
Occupancy of 0,0,0	0.5	0.0	0.3
Si1/P1-Si1/P1	2.92	3.032	2.966
Si1/P1-Si2/P2	3.20	n.a.	3.123
Si2/P2-Si2/P2	2.55	2.576	2.547
Ti1-Si1/P1	2.56	2.634	2.558
Ti1-Ti1	2.54	2.576	2.547
Ti1-Ti2	3.11	n.a.	3.060
Ti2-Si1/P1 (I)	2.56	2.785	2.768
Ti2-Si1/P1 (II)	2.62	2.658	2.603
Ti2-Si1/P1 (III)	2.56	2.570	2.493
Ti2-T2 (I)	3.02	3.184	3.063
Ti2-T2 (II)	3.08	3.242	3.100
Ti2-Si2/P2	**2.16**	**2.272**	**2.179**

Note: n.a. – not available. Bold indicate an unusually short bond. Source of data: (1) This study; (2) Williams et al. (2000b); (3) Lundström and Snell (1967)

Table 6. Coordinates and equivalent displacement parameters (U_{iso} Å^2) of atoms in kangjinlaite

Label	x/a	y/b	z/c	U_{iso}	occupancy	multiplicity
Ti1	0.1811(3)	0.1811(3)	0	0.005	1	8
Ti2	0.5	0.1654(3)	0.10097(16)	0.005	1	16
Ti3	0.2509(3)	0	0.18651(15)	0.005	1	16
Ti4	0.5	0.5	0.1661(3)	0.005	1	4
Si1	0.3720(4)	0.3720(4)	0	0.005	0.74	8
P1	0.3720(4)	0.3720(4)	0	0.005	0.26	8
Si2	0	0	0.1030(5)	0.005	0.74	4
P2	0	0	0.1030(5)	0.005	0.26	4
Si3	0.2937(3)	0.2937(3)	0.1742(2)	0.005	0.74	16
P3	0.2937(3)	0.2937(3)	0.1742(2)	0.005	0.26	16
Si4	0.3595(6)	0	0	0.005	0.74	8
P4	0.3595(6)	0	0	0.005	0.26	8
Si5	0.5	0	0.25	0.005	0.74	4
P5	0.5	0	0.25	0.005	0.26	4

Table 7. Comparison of kangjinlaite with Si-rich compounds isostructural with $Ho_{11}Ge_{10}$.

	Kangjinlaite	Synthetic	Synthetic
Source	this study	Kotur et al. (1985)	Zhao et al. (1988)
Ideal formula	$Ti_{11}(Si,P)_{10}$	$Sc_{10}Cr_{(4+x)}Si_{(10-x)}$ x= 0.8	$Sc_7Re_{(4-x)}Si_{(10+x)}$ [x = 0.65]
Space group	*I4/mmm*	*I4/mmm*	*I4/mmm*
a Å	9.4	9.757	9.8123
c Å	13.5	13.884	14.274
V Å^3	1190	1321.7	1374.3
Z	4	4	4
Si1-Si1 Å	2.41	2.3827	2.189
Si1-Si3 Å	2.57	2.5953	2.815
Si2-Si2 Å	2.78	2.999	2.89
Si3-Si3 Å	2.35	2.3690	2.516
Si4-Si4 Å	2.64	2.598	2.49
Ti1-Ti1 Å	3.41	3.4891	3.631
Ti1-Ti2 Å	3.30	3.481	3.451
Ti1-Ti3 Å	3.11	3.2266	3.281
Ti2-Ti2 Å	2.73-3.11	3.452	3.050
Ti2-Ti3 Å	2.98-3.04	3.010	3.063
Ti2-Ti4 Å	3.27	3.2679	3.372
Ti3-Ti4 Å	3.08	3.2270	3.264

1056

1057 Figure 1. High-angle annular dark-field scanning-transmission electron microscope (HAADF-

1058 STEM) image of foil #5358 showing an aggregate of zhiqinite, $TiSi_2$, several of which have a

1059 tabular habit, enclosing globules of TiP and surrounded by wenjiite ($Ti_{10}(Si,P)_7$) and kangjinlaite

1060 $Ti_{11}(Si,P)_{10}$. Al_2O_3 – corundum hosting the Ti silicide inclusion. Two of the four EDX chemical

1061 analyses and the 3-dimensional electron diffraction (3D ED) data of wenjiite were collected on a

1062 single crystal within the area marked by the large white square or very close. The analyzed area

1063 is exactly the same for EDX and 3-dimensional electron diffraction because there is a complete

1064 crystallographic continuity in the immediate vicinity of the square; that is, the analyses were

1065 obtained on the same crystal. Two more analyses were obtained a short distance away (small

1066 white squares). White filled circle indicates where electron diffraction data were collected for

1067 kangjinlaite. Numbered unfilled black circles indicate the two areas where chemical data were

1068 obtained. The boundary between wenjiite and kangjinlaite is marked by a thick white line since it

1069 is not otherwise visible. The image was obtained at the Istituto Italiano di Tecnologia. Insert

1070 shows enlargement of the spheroid composed of wenjiite ($Ti_{10}(Si,P)_7$) and kangjinlaite

1071 ($Ti_{11}(Si,P)_{10}$ (white) and $TiSi_2$ (zhiqinite, gray). Image taken at the Center for Advanced

1072 Research on the Mantle, Beijing. Figure is modified from Figures 2 and 3(b) in Xiong et al.

1073 (2020).

1074
1075 Figure 2. High-angle annular dark-field scanning-transmission electron microscope (HAADF-

1076 STEM) image of foil #6034 showing a lamellar intergrowth of khamrabaevite-osbornite,

1077 Ti(C,N), deltalumite, (Al, Mg, □)Al_2O_4, jingsuiite, TiB_2 and wenjiite. A K-bearing

1078 dmisteinbergite-like mineral occurs in two interstices in the intergrowth. Al_2O_3 indicates the

1079 corundum hosting the lamellar intergrowth. Areas analyzed at the Istituto Italiano di Tecnologia

1080 are marked by squares. 3-dimensional electron diffraction data were also obtained at C46 and

1081 gave the same cell and extinctions as wenjiite in foil #5358. The image was obtained at the GFZ

1082 German Research Centre for Geosciences. Figure is modified from Figure 6(b) in Xiong et al.

1083 (2022)

1084
1085 Figure 3. Backscattered electron image of foil #G7708 showing the occurrence of wenjiite with

1086 osbornite, jingsuiite and an unidentified oxide included in corundum. The image was obtained at

1087 the Institute of Geology, Chinese Academy of Geological Sciences.

1088
1089 Figure 4. Diagram of the compositional ranges and averages for kangjinlaite and wenjiite in foils

1090 #5358 and #6034 in the ternary system P-Si-Ti (a), expressed in terms of the idealized end-

1091 member components $Ti_{10}P_6$, $Ti_{10}Si_6$, $Ti_{11}P_{10}$ and $Ti_{11}Si_{10}$, in which V, Cr, Mn and Fe are included

1092 with Ti (b). Sources for data from the literature: single-crystal structure refinements (SREF) of

1093 synthetic $Ti_{10}P_6$ (Bärnighausen et al. 1965, Lundström and Snell 1967); range of synthetic $Ti_{10}P_6$

1094 (Okamoto 2007), and range of synthetic $Ti_{10}Si_6$ (Svechnikov et al. 1970; Fiore et al. 2016).

1095
1096 Figure 5. Three-dimensional reconstruction of electron diffraction data taken from wenjiite, $Ti_{10}(Si,P,\square)_7$,

1097 in the area enclosed in the white square in foil #5358 (Fig. 1). (a) View along [100]*, with extinction

1098 obeying the rule $0k\ell$: $\ell = 2n$ highlighted by pink arrows. (b) View along [001]*. (c) View along [110]*,

1099 which shows no evidence for the $hh\underline{-2h}\ell$ extinction rule. This limits the possible space groups to $P63cm$

1100 (#185), $P\text{-}6c2$ (#188) and $P6_3/mcm$ (#193). Cell edges are yellow. Red vectors indicate a^* direction, green

1101 vectors indicate b^* direction and blue vectors indicate c^* direction. Note that those are projections of a

1102 three-dimensional reconstruction and not two-dimensional electron diffraction patterns. Therefore,

1103 panels are indicated as [100]*, [001]* and [110]* and not as $0kl$, $hk0$ and $h\underline{-h}0$, and planar

1104 extinctions appear as projected columns of extinct reflections. Data were obtained at the Istituto Italiano

1105 di Tecnologia.

1106
1107   Figure 6. Crystal structure of wenjiite. (a) View along a; (b) view along c.

1108
1109   Figure 7. Three-dimensional reconstruction of electron diffraction data taken from kangjinlaite,

1110 $Ti_{11}(Si,P)_{10}$, from the white filled circle in foil #5358 (Fig. 1). (a) View along [100]*. (b) View along

1111   [010]*. (c) View along [001]*. (d) View along [110]*, showing chess-board extinctions due to the *I*-

1112   centered lattice. Cell edges are sketched in yellow. Red vectors indicate *a** direction, green vectors

1113   indicate *b** direction and blue vectors indicate *c** direction. Note that those are projections of a three-

1114   dimensional reconstruction and not two-dimensional electron diffraction patterns. Therefore, panels are

1115   indicated as [100]*, [010]*, [001]* and [110]* and not as 0*kl*, *h*0*l*, *hk*0 and *h*-*h*0, and planar

1116   extinctions appear as projected columns of extinct reflections. Data were obtained at the Istituto Italiano

1117   di TecnologiaData were obtained at the Istituto Italiano di Tecnologia.

1118
1119   Figure 8. Crystal structure of kangjinlaite. A. View along c. Note square array of Si1 atoms (blue

1120   outline and lettering), which lies below the surface. B. View along a.

1121
1122   Figure 9. The Periodic Table showing the 38 elements reported in compounds isostructural with

1123 $Ho_{11}Ge_{10}$, including kangjinlaite.

1124
1125   Figure 10. Plot of equivalents of Ti1 – Ti3 bond length in kangjinlaite in 55 compounds of the

1126 $Ho_{11}Ge_{10}$ type, which are isostructural with kangjinlaite. The three most compact structures

1127   reported to date are labelled as containing Si or Mn. The literature sources of data are given in

1128   Appendix II.

1129
1130
1131   Figure 11. (a) Plot of compounds in the ternary Ti–Si–P system in foil no. 5358 (modified from

1132   Figure 9 in Xiong et al. 2020). Source of compositional data: badengzhuite and zhiqinite (Xiong

1133   et al. 2020); wenjiite and kangjinlaite (Tables 1 and 3). Compositions for synthetic Ti–Si phases

1134   are from Fiore et al. (2016). Red is tie line for badengzhuite-zhiqinite . Red arrow shows inferred

1135   crystallization sequence for the ternary melt yielding the spheroid in foil no. 5358. (b) Plot of

1136   compounds in the binary Ti–Si system in foil no. 5358 (modified from Figure 10(a) in Xiong et

1137   al. 2020). Temperatures for melting in the Ti-Si binary are taken from Fiore et al. (2016) except

1138   for kangjinlaite, which Fiore et al. (2016) did not report.

1139

1140   Figure 12. List of 15 systems in which structures of the $Ho_{11}Ge_{10}$ and Mn_5Si_3 type are both

1141   reported. For Y-Ge, two phases melt congruently. Intervening phases have compositions between

1142   Ho:Ge = 11:10 and Ho:Ge = 5:3. Sources: Ti-Si (Fiore et al. 2016); Sc-Ge (Okamoto 2014); Y-

1143   Ge (Okamoto 2015); Tb-Ge (Eremenko et al. 1988); Ho-Ge (Eremenko et al. 1980); Er-Ge

1144   (Achgar et al. 2017); Tm-Ge (Achgar et al. 2018b); Yb-Ge (Achgar et al. 2018c), Lu-Ge (Achgar

1145   et al. 2018a); Eu-As (Taylor et al. 1978; Wang et al. 1978), Y-Sn (Okamoto 2013a, compare

1146   Iddoudi et al. 2013); Ca-Sb (Okamoto (2016, compare Zaitsev et al. 1997); Eu-Sb (Okamoto

1147   2013b); Yb-Sb (Okamoto 2013a); Sr-Bi (Wang et al. 2014, Grew 2021) and (Yb-Bi (Okamoto

1148   2016).
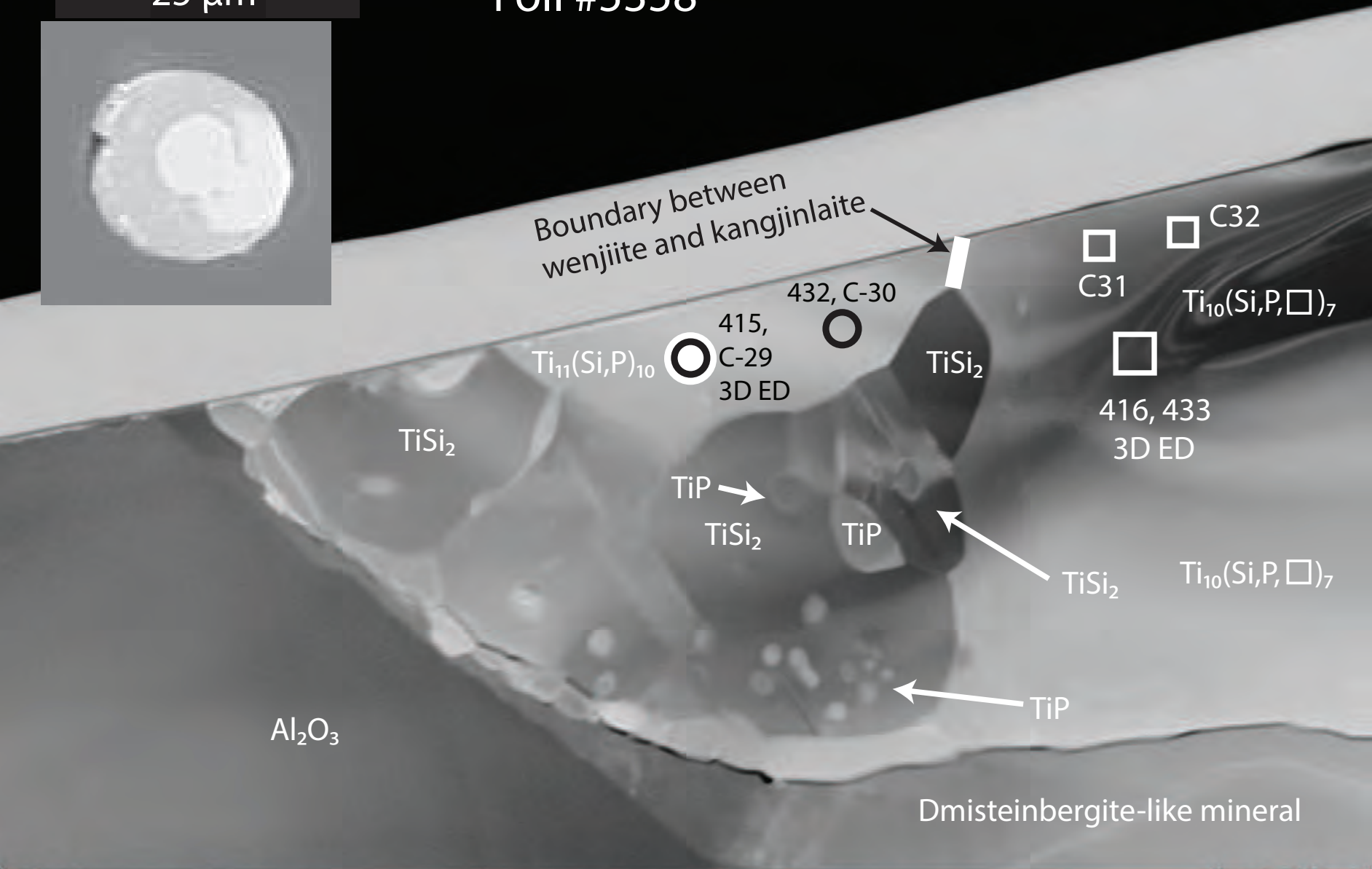
50

Figure 1

Foil #5358

Foil #6034

Figure 2

Al₂O₃

Khamrabaevite-
osbornite
Ti(C,N)

Al₂O₃

C 48

TiB₂

K-bearing
dmisteinbergite-
like mineral

C 46 & 3D ED

Wenjiite

Jingsuiite
TiB₂

C 47

Al₂O₃   Ti(C,N)

C 45

Deltalumite

TiB₂

3 μm
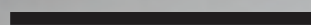
1 um
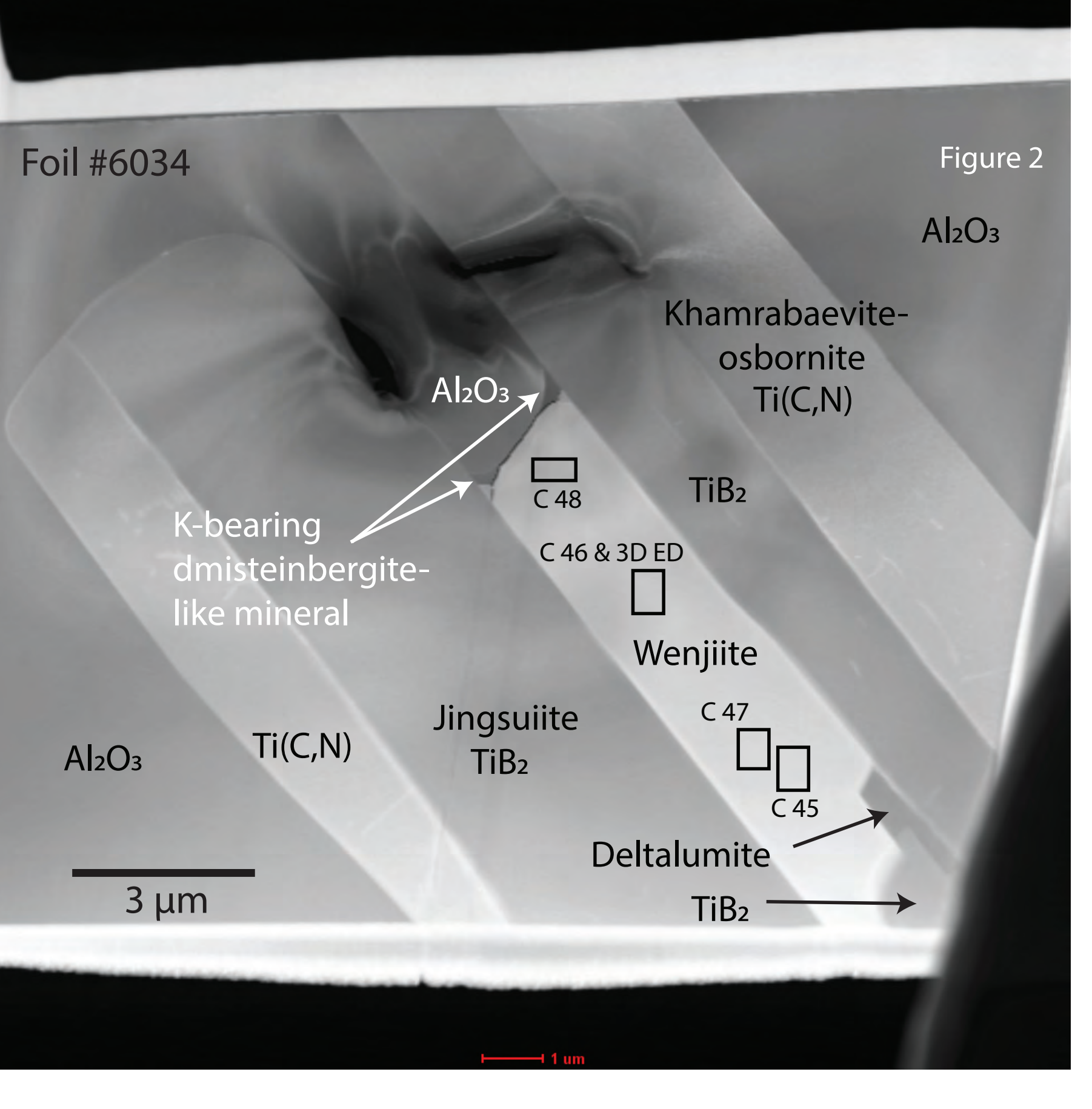
Foil #G7708

Corundum

Osbornite

Wenjiite

Ti-Zr-Al-Si oxide

Jingsuiite

Corundum

Figure 3

HV	WD	mag	det	curr	HFW
20.00 kV	11.2 mm	1 781 x	CBS	0.11 nA	116 µm

⊢————————— 40 µm —————————⊣

Versa 3D

Figure 4

(a)

(b)

(a) [100]*   (b) [001]*   (c) [110]*

Figure 6

(a) [100]*

(b) [010]*

(c) [001]*

(d) [110]*
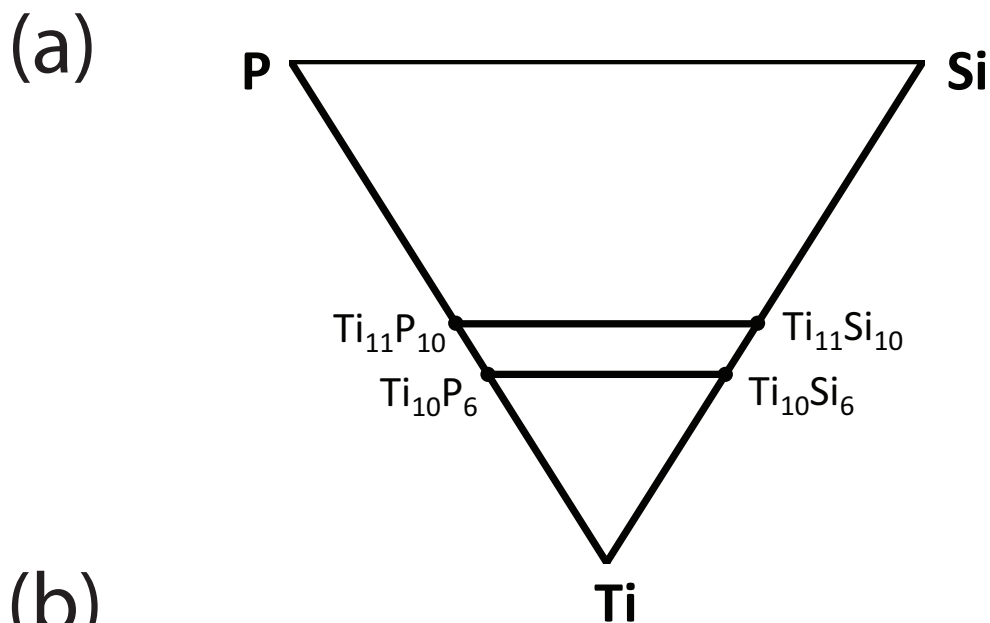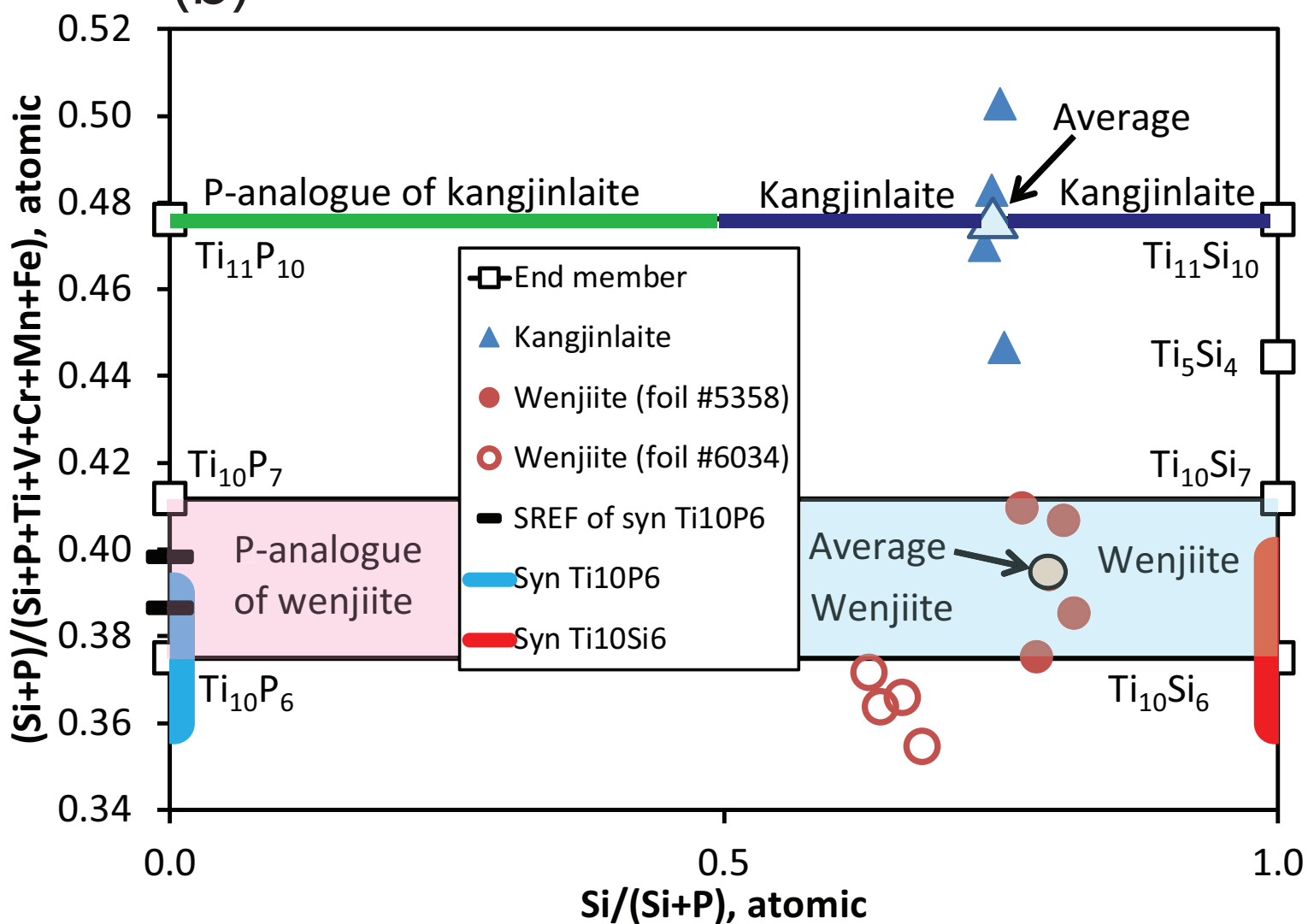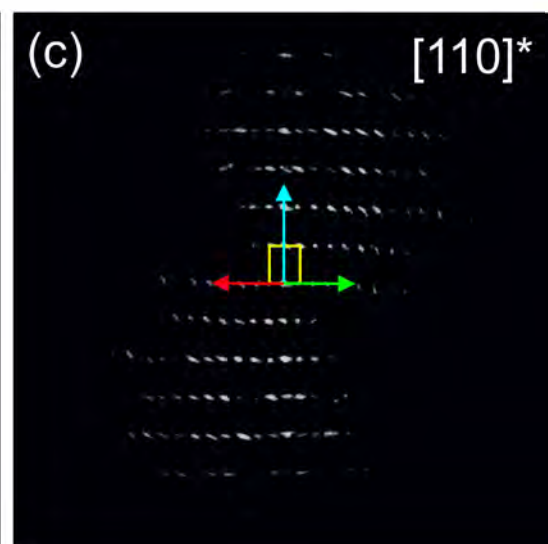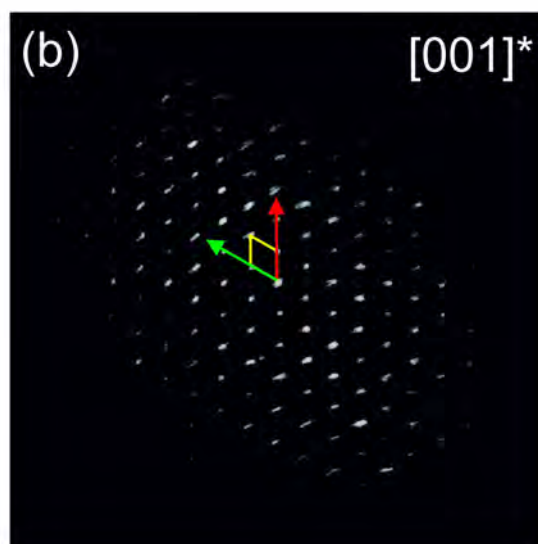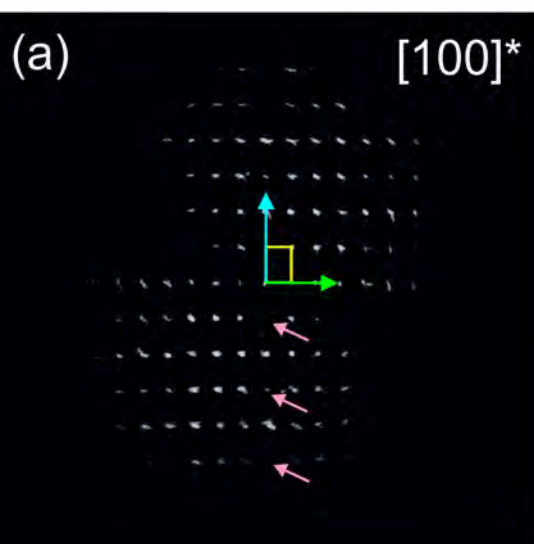
Figure 8
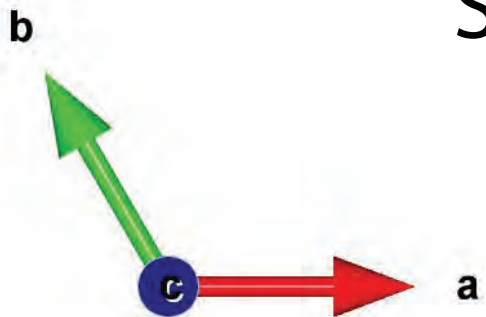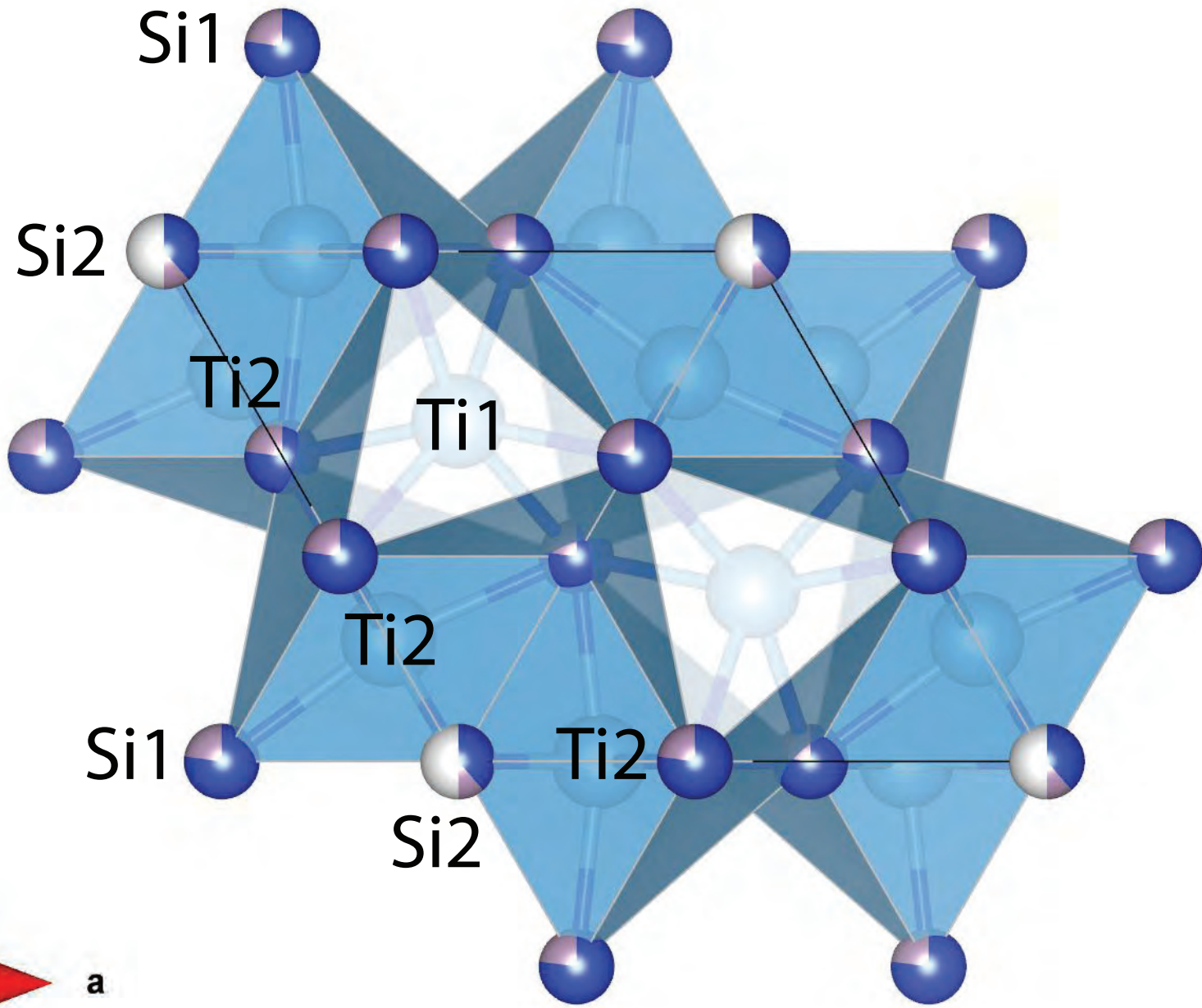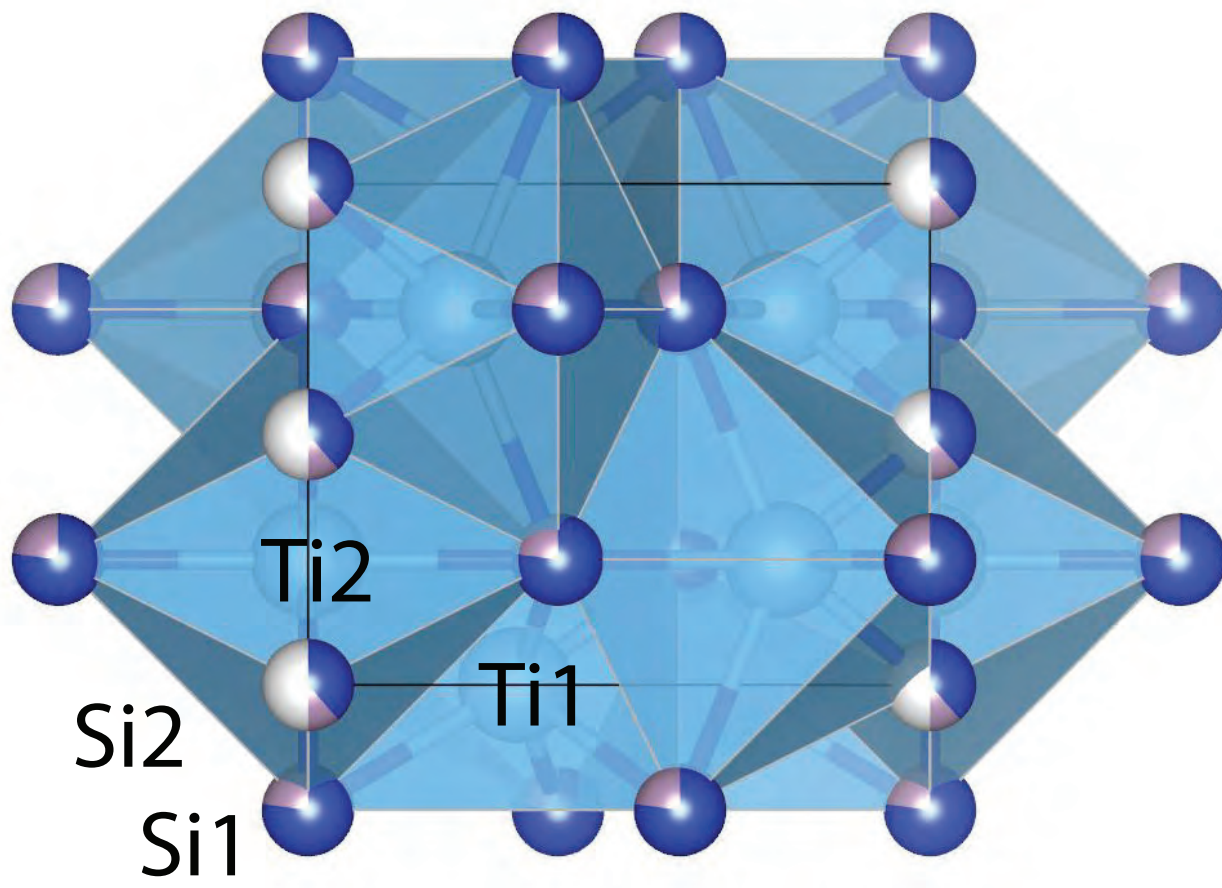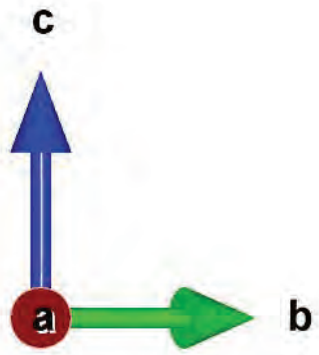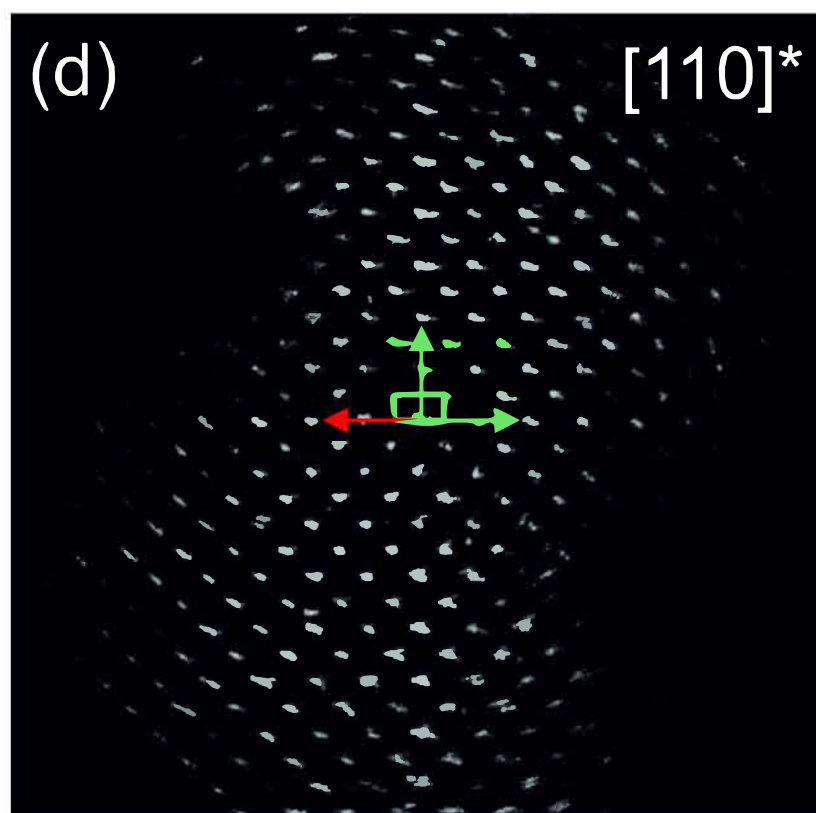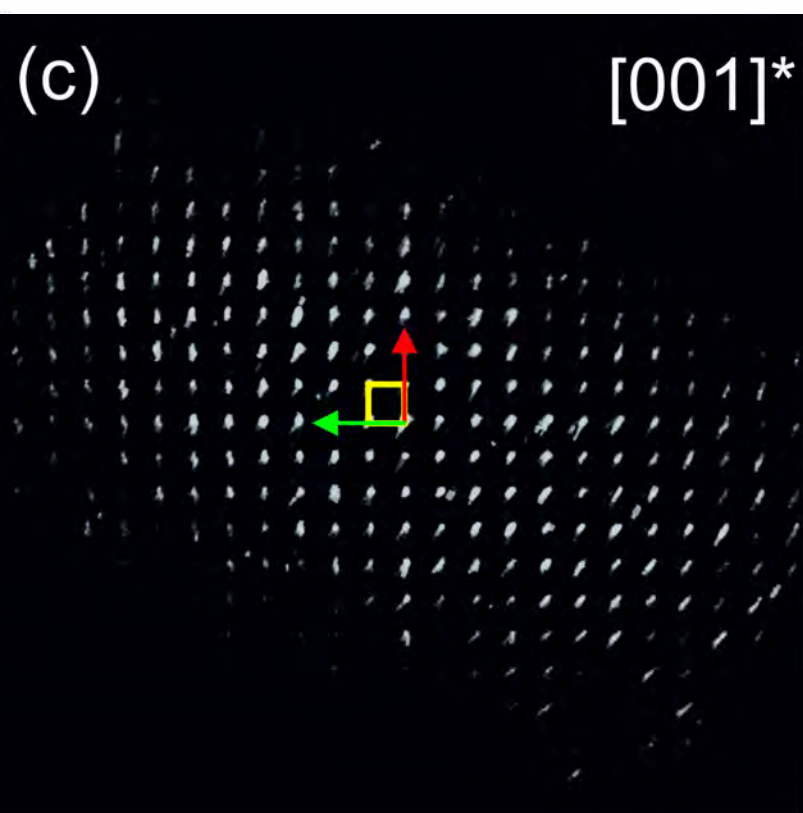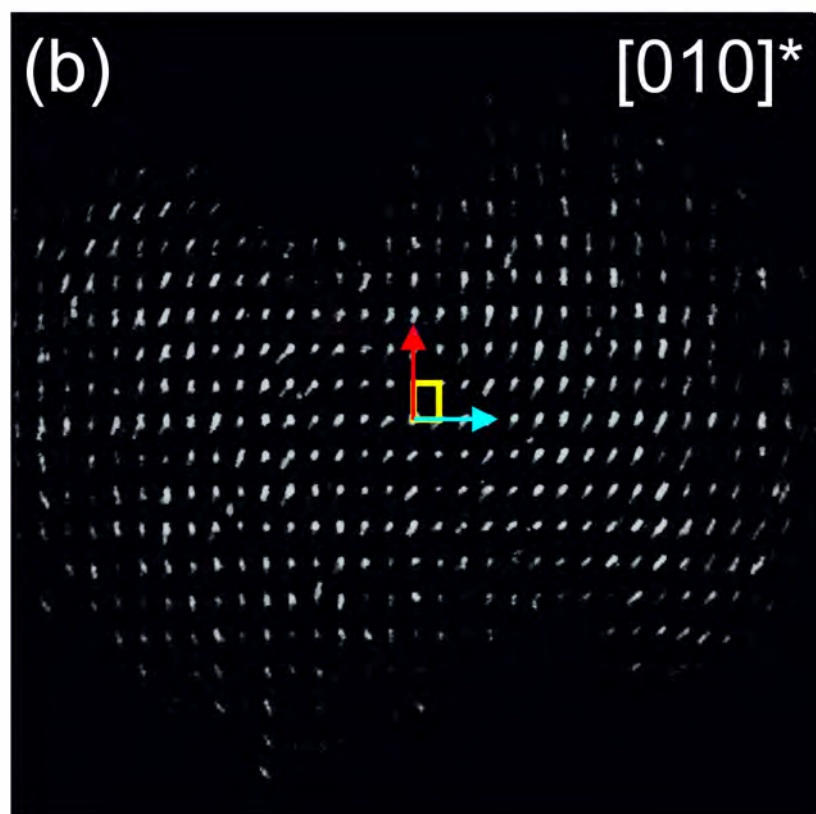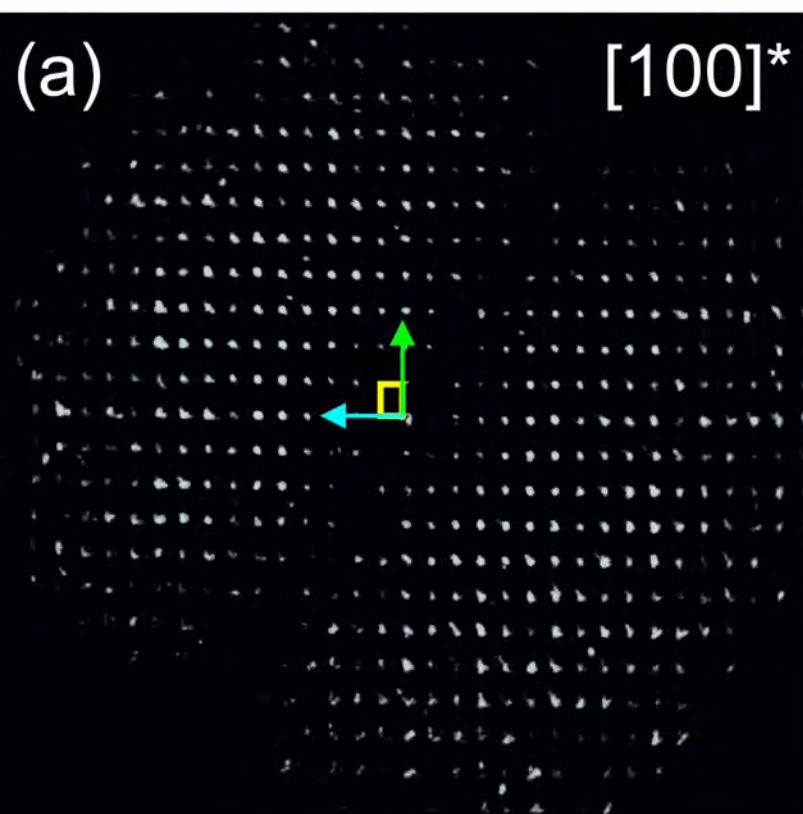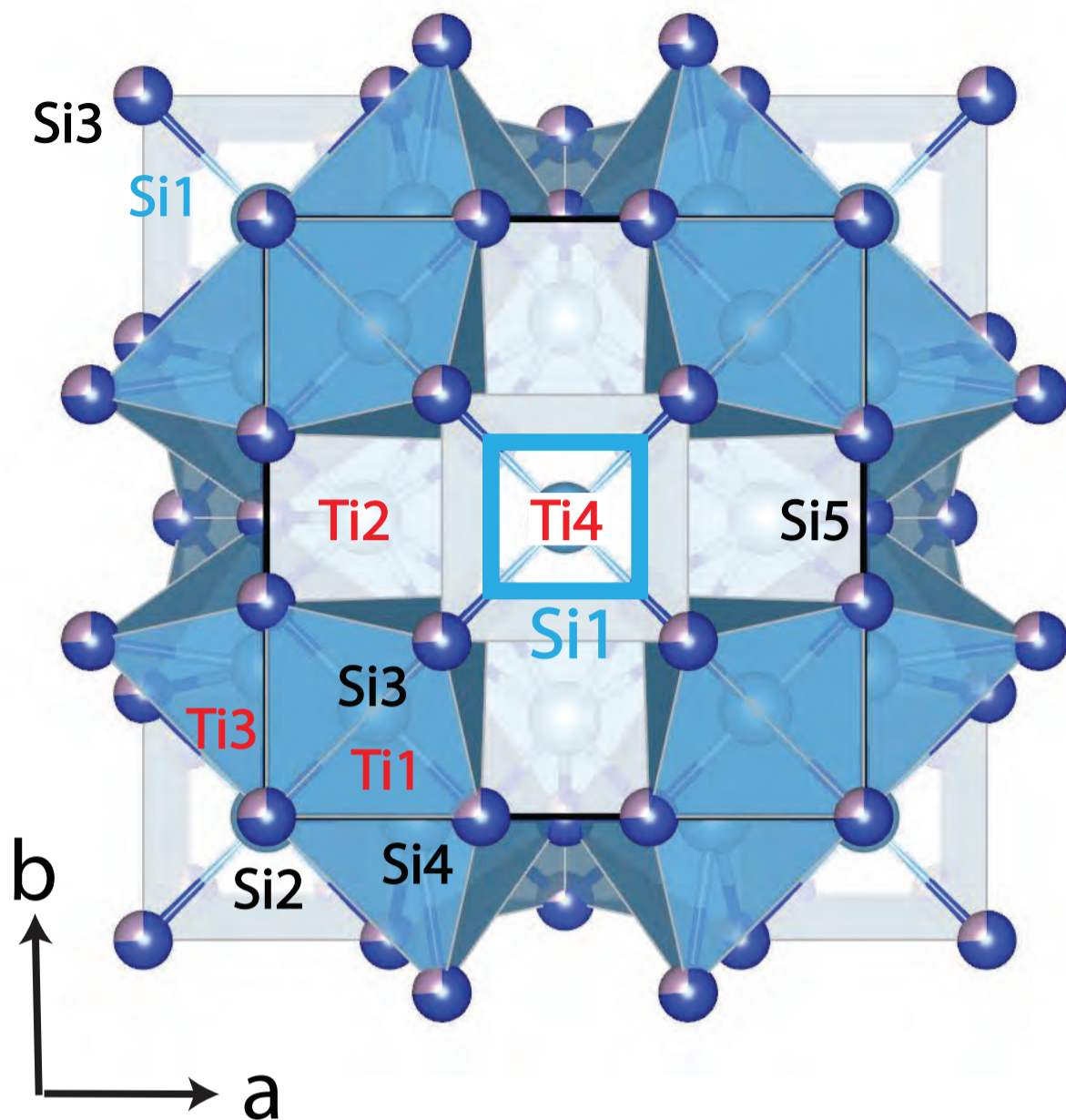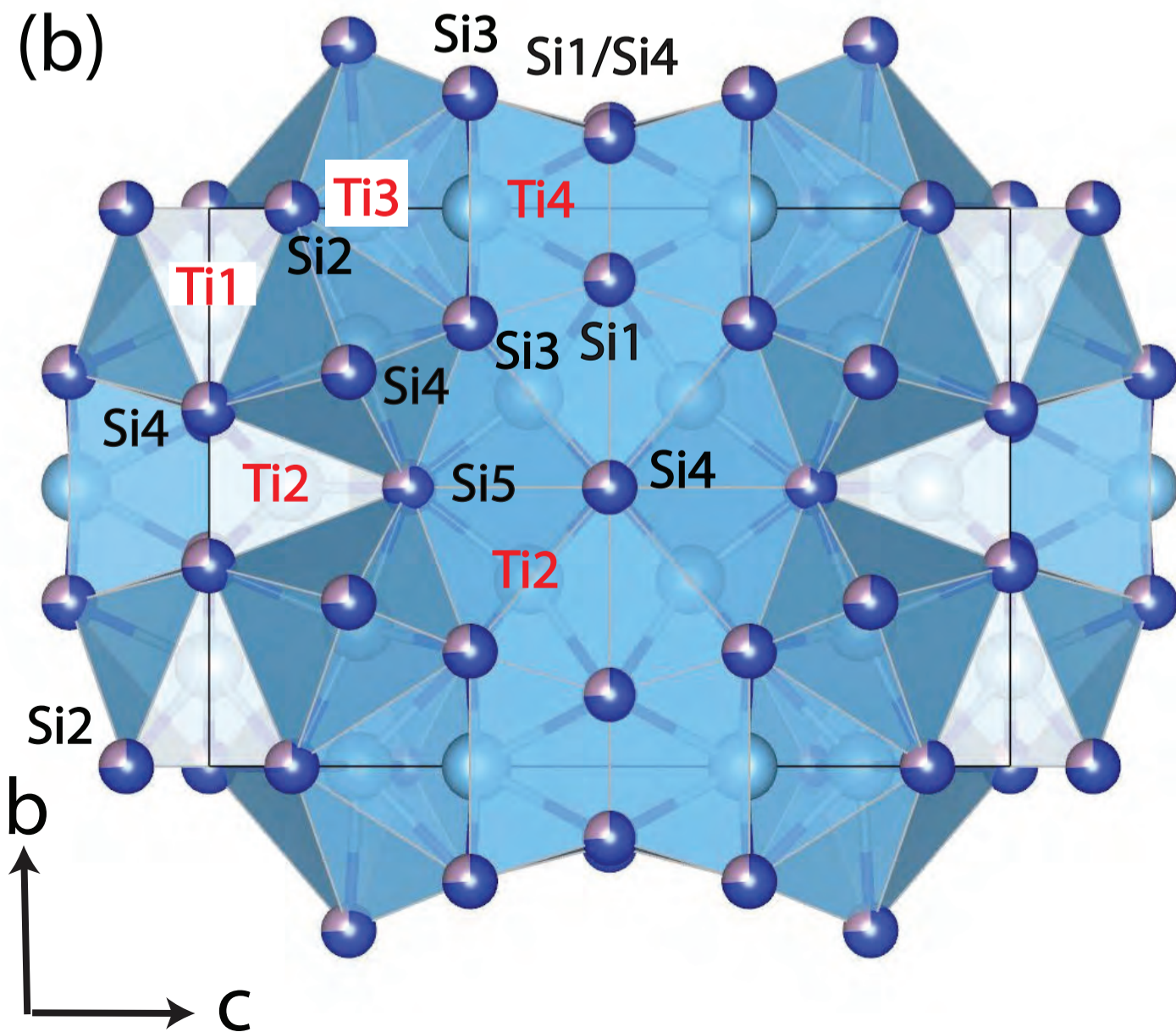
H																	He
Li	Be											B	C	N	O	F	Ne
Na	Mg											Al	Si	P	S	Cl	Ar
K	Ca	Sc	Ti	V	Cr	Mn	Fe	Co	Ni	Cu	Zn	Ga	Ge	As	Se	Br	Kr
Rb	Sr	Y	Zr	Nb	Mo	Tc	Ru	Rh	Pd	Ag	Cd	In	Sn	Sb	Te	I	Xe
Cs	Ba	La	Hf	Ta	W	Re	Os	Ir	Pt	Au	Hg	Tl	Pb	Bi	Po	At	Rn
Fr	Ra	Ac															
			Ce	Pr	Nd	Pm	Sm	Eu	Gd	Tb	Dy	Ho	Er	Tm	Yb	Lu	
			Th	Pa	U												

Reported as an occupant at the Ho site
Reported as an occupant at the Ge site
Reported as an occupant at both sites
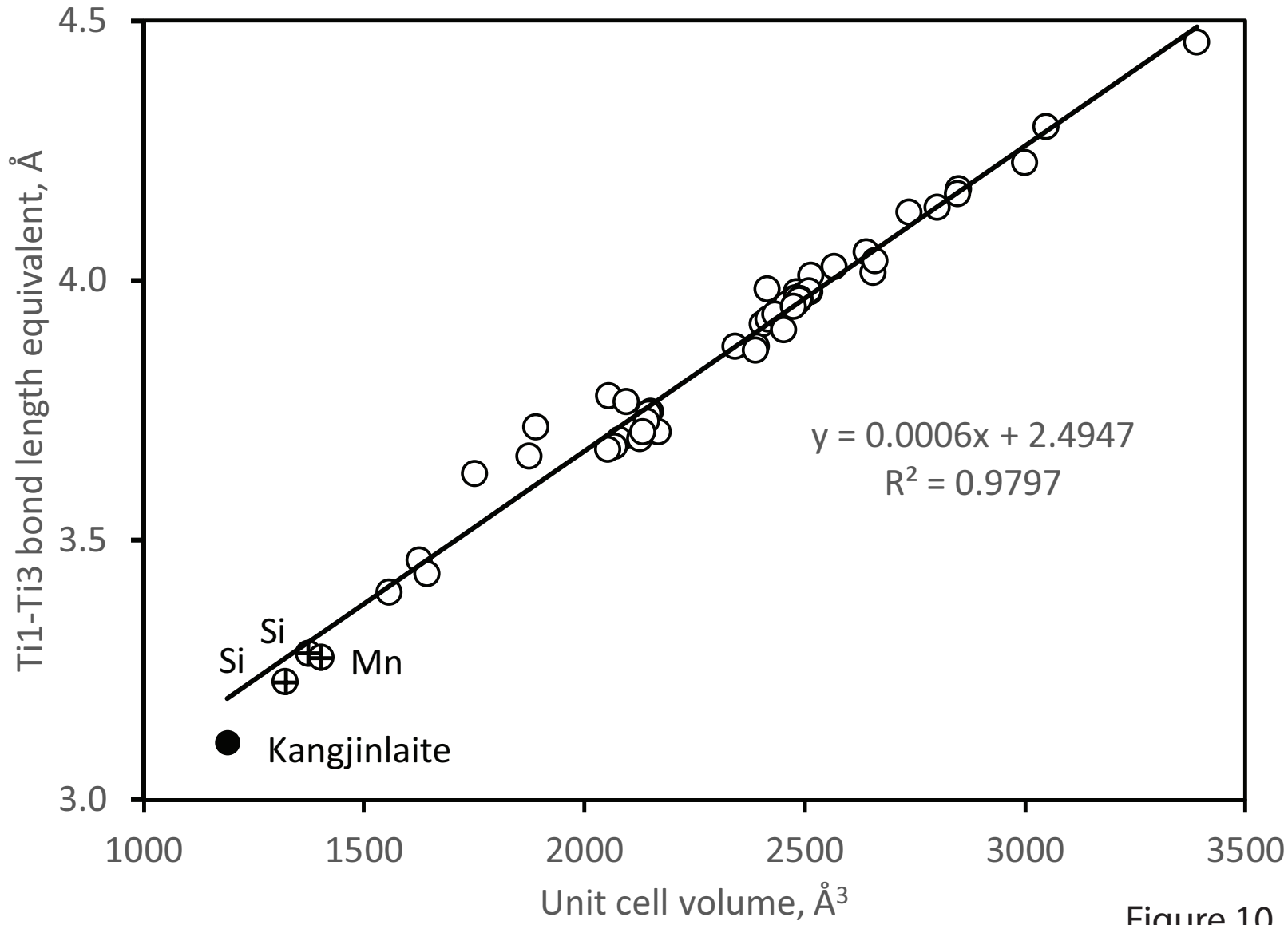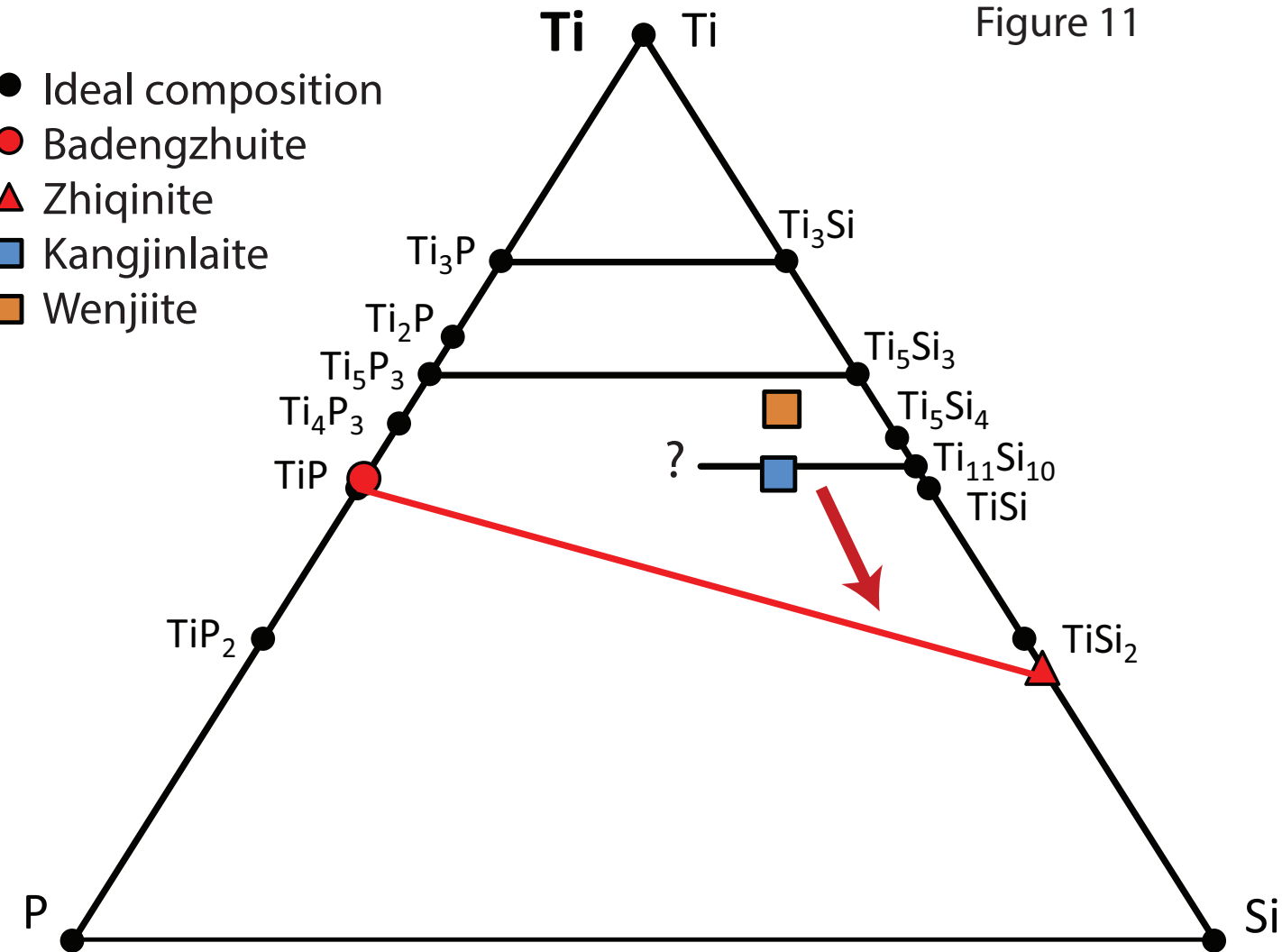Reported only in kangjinlaite
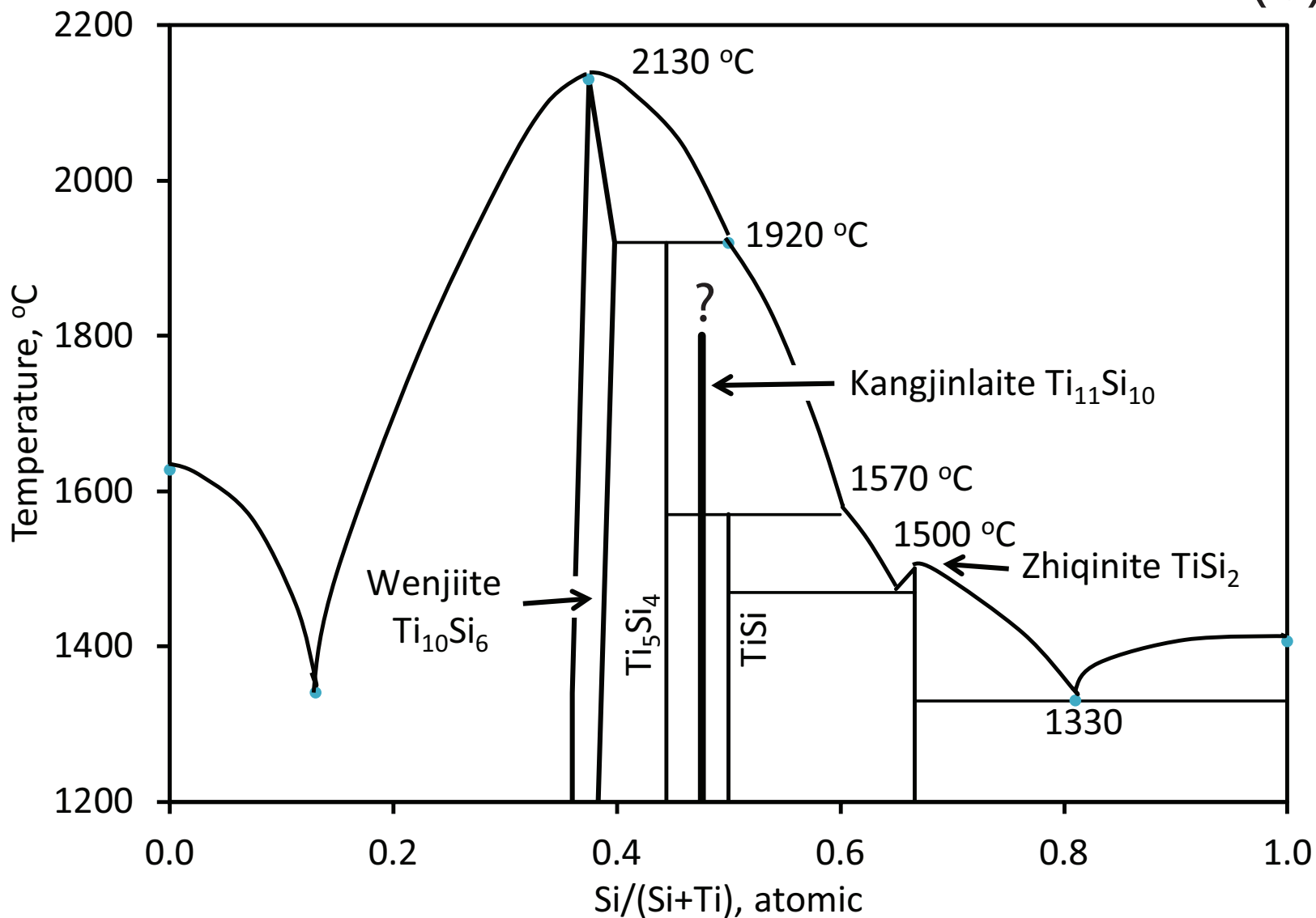Reported only in $Eu_{11}As_{10}$

Figure 9

Figure 10

Figure 11

(a)

Ti

- Ideal composition
- Badengzhuite
- Zhiqinite
- Kangjinlaite
- Wenjiite

Ti₃P
Ti₂P
Ti₅P₃
Ti₄P₃
TiP
?
TiP₂

Ti₃Si
Ti₅Si₃
Ti₅Si₄
Ti₁₁Si₁₀
TiSi
TiSi₂

P

Si

P

Si

(b)

2130 °C
1920 °C
?
Kangjinlaite Ti₁₁Si₁₀
1570 °C
1500 °C
Zhiqinite TiSi₂
Wenjiite Ti₁₀Si₆
Ti₅Si₄
TiSi
1330

Temperature, °C

Si/(Si+Ti), atomic

Ho position	Ge position	Intervening phase	Liquidus T (°C) $Ho_{11}Ge_{10}$ type	Liquidus T (°C) Mn_5Si_3 type
Ti	Si	P-Ti_5Si_4 (two polymorphs)	P < 1920	C-2130
Sc	Ge	P-Sc_5Ge_4 (Sm_5Ge_4 type)	P-1668	C-2061
Y	Ge	C-Y_5Ge_4 (Sm_5Ge_4 type) at 1941 °C	P-1884	C-1968
Tb	Ge	P-Tb_5Ge_4 (Sm_5Ge_4 type)	P-1660	C-1800
Ho	Ge	P-Ho_5Ge_4 (Sm_5Ge_4 type)	P-1700	C-1950
Er	Ge	P-Er_5Ge_4 (Sm_5Ge_4 type)	P-1719	C-1954
Tm	Ge	P-Tm_5Ge_4 (Sm_5Ge_4 type)	P-1722	C-1960
Yb	Ge	C-Yb_5Ge_4 (Sm_5Ge_4 type) at 1642 °C	P-1505	P-1581
Lu	Ge	P-Lu_5Ge_4 (Sm_5Ge_4 type)	P-1719	C-2044
Eu	As	Eu_5As_4 to 1402 °C	>1402	1502
Y	Sn	P-Y_5Sn_4 (Sm_5Ge_4 type)	P-1603	C-1940
Ca	Sb	none found	C-1127	P-880
Eu	Sb	P-Eu_5Sb_4, C-$Eu_{16}Sb_{11}$	P-950	P-1445
Yb	Sb	C-Yb_4Sb_3 at 1680 °	P-1405	P-1540
Sr	Bi	C-Sr_5Bi_3 (Yb_5Sb_3 type) at 945 °C	P-610	P-700
Yb	Bi	C-Yb_4Bi_3 at 1480 °C	P-900	P-1400
P = peritectic melting	C = congruent melting			Figure 12